THESIS FOR THE DEGREE OF DOCTOR OF PHILOSOPHY IN
THERMO AND FLUID MECHANICS

Vehicle wakes in side wind

MAGNUS URQUHART

Department of Mechanics and Maritime Sciences
Division of Vehicle Engineering and Autonomous Systems
CHALMERS UNIVERSITY OF TECHNOLOGY
Göteborg, Sweden 2021

Vehicle wakes in side wind
MAGNUS URQUHART
ISBN 978-91-7905-564-6

Doktorsavhandlingar vid Chalmers tekniska högskola
Ny serie nr. 5031
ISSN 0346-718X

Department of Mechanics and Maritime Sciences
Chalmers University of Technology
SE–412 96 Göteborg
Sweden
Telephone: +46 (0)31–772 1000

Chalmers Reproservice
Göteborg, Sweden 2021

"The Force will be with you. Always" - Obi-Wan Kenobi

Vehicle wakes in side wind

Magnus Urquhart
Department of Mechanics and Maritime Sciences
Chalmers University of Technology

Abstract

There is a global push to reduce the energy consumption of passenger vehicles with increasingly stringent targets and regulations. More than one-tenth of Europe's greenhouse gasses are due to passenger vehicles. The aerodynamic drag is a major contributor to energy consumption responsible for more than a quarter of the vehicle's energy usage. Thus, improving the aerodynamic drag will help us achieve our greenhouse gas emissions targets.

Vehicle aerodynamics is typically assessed and developed in idealised conditions using low turbulence wind tunnels and numerical methods. Several aspects influencing vehicle aerodynamics are often neglected such as traffic and wind conditions. This thesis explores the effects of steady wind, or yawed flow, on the wake of vehicles. The goal is to increase the knowledge of the full wake behaviour at yaw and how it is related to the aerodynamic drag. For this, an optimisation method is used throughout this work to generate robust, low-drag, reference geometries. The optimisation is done at different yaw angles, allowing asymmetric geometries at yaw. The cycle averaged drag, which takes into account the driving cycle as well as the wind distribution, is also considered to create symmetric geometries which are insensitive to yaw. The optimisation is focused on base cavities and trailing edge modifications to these cavities.

Generally, the low-drag configurations have a more balanced wake, with and without side wind, where the recirculating flow in the wake is aligned with the vehicle. The improved balance allows the wake to move more freely which often increases the large scale coherent motions of the wake. These unsteady motions are linked to increases in drag in the literature, however, in this work, improving the wake balance was found to be the more important indicator of the overall drag. At yaw, the coherent unsteady motions are reduced as a result of the wake being locked in a more stable, but higher drag, upwash or downwash dominated state.

The wake becomes increasingly downwash or upwash dominated at yaw by a large rotating structure in the wake. The yaw insensitive designs have a wake that is slightly biased towards the top or bottom of the base at zero yaw to counteract the movement of the wake at yaw. Optimising the geometry without considering yaw can reduce the performance over the entire operating range. This highlights the importance of considering several operating conditions during vehicle development.

Keywords: aerodynamics, cavity, yaw, drag, wake, CFD, tomographic PIV, crossflow, wind, optimization, surrogate model

Acknowledgements

I am grateful for the support and guidance I have received from Prof. Simone Sebben, you have always been encouraging me to reach further. This project was done in collaboration with the Volvo Car Corporation. The people at Volvo have been very helpful throughout this work, providing support and discussing ideas. A special thanks goes out to my supervisors Alexander Broniewicz, Lennert Sterken and Teddy Hobeika.

A significant amount of this work was made possible thanks to the collaboration with the kind people at Loughborough University. Max Varney dedicated a lot of his time and effort to prepare and run wind tunnel experiments while being in the final stages of his thesis, for this I am thankful. Thank you Matthew Ward for helping us run and setup the PIV experiments. Finally, I would like to express my gratitude to Prof. Martin Passmore for facilitating the research collaboration and the time spent working on our joint papers.

This project was financed by the Swedish Energy Agency within the program of Transport, Energy efficient vehicles. The simulations were performed on the computational cluster at Volvo Car Corporation and resources provided by the Swedish National Infrastructure for Computing (SNIC).

Thanks to my family who have been supportive and encouraged me on this journey. To my fiancée Sofia, you have always been there to support me through both the easier and harder times, for that, I am very grateful. And to my cats and home office colleagues Leia and Spiken, you constantly have my well being in mind, reminding me to take breaks, thank you.

Finally, I would like to mention my colleagues and friends at VEAS. The great work environment and all the activities outside of work has made this endeavour a pleasure to share with all of you. To the people in the RVAD group, the many discussions and the open atmosphere has taught me a lot about aerodynamics and has been very rewarding. Special thanks to Sonja at VEAS, you always have our best interest in mind.

Nomenclature

F_{D}	Drag force	[N]
C_{D}	Drag coefficient	[-]
C_{L}	Lift coefficient	[-]
C_{FL}	Front lift coefficient	[-]
C_{RL}	Rear lift coefficient	[-]
C_{S}	Side force coefficient	[-]
C_{Yaw}	Yaw moment coefficient	[-]
Θ	Yaw angle	[°]
C_{DWC}	Cycle averaged drag coefficient	[-]
C_{DB}	Base drag coefficient	[-]
C_{MB}	Base moment coefficient	[-]
P	Static pressure	[Pa]
C_{P}	Pressure coefficient	[-]
C_{Ptot}	Total pressure coefficient	[-]
$F_{\mathrm{resistive}}$	Total resistive driving force	[N]
$\theta_{\mathrm{incline}}$	Road inclination angle	[rad]
F_{RR}	Rolling resistance	[N]
ξ	Flow variable such as pressure or velocity	[N.A.]
ξ_{∞}	Subscript of freestream flow property ξ	[N.A.]
ξ_{RMS}	Subscript of Root Mean Square of property ξ	[N.A.]

ξ'	Superscript of fluctuating flow property ξ	[N.A.]
$\overline{\xi}$	Time-average of flow property ξ	[N.A.]
V	Velocity	[m/s]
L	Vehicle length	[m]
ρ	Density	[kg/m^3]
C_{Courant}	Courant number	[-]
v_{cell}	Cell volume	[m^3]
A	Projected frontal area	[m^2]
St	Strouhal number	[-]
f	Frequency	[Hz]
y^+	Non-dimensional first cell center height	[-]
ν	Kinematic viscosity	[m^2/s]
μ	Dynamic viscosity	[kg s/m]
$C_\xi(x_A, x_B)$	Two-point correlation between points x_A and x_B	[N.A.]
ξ_{RBF}	Radial Basis Function	[N.A.]
ε	Radial Basis Function width	[N.A.]
w_i	Radial Basis Function weight	[N.A.]
c_j	Axis scaling factor of j-th design dimension	[-]

Abbreviations

GHG	Greenhouse Gas
NEDC	New European Driving Cycle
WLTP	Worldwide Harmonised Light vehicle Test Procedure
WLTC	Worldwide Harmonized Light vehicle Test Cycle
CFD	Computational Fluid Dynamics
RANS	Reynolds Averaged Navier Stokes
LES	Large Eddy Simulation
IDDES	Improved Delayed Detached Eddy Simulation
PIV	Particle Image Velocimetry
HFSB	Helium Filled Soap Bubbles
POD	Proper Orthogonal Decomposition
LHC	Latin Hypercube
RBF	Radial Basis Function

Thesis

This thesis consists of an extended summary of five papers, listed below.

I. Urquhart M., Sebben S. and Sterken L., *Numerical analysis of a vehicle wake with tapered rear extensions under yaw conditions.* In: Journal of Wind Engineering and Industrial Aerodynamics, Volume 179, Pages 308-318, ISSN 0167-6105, 2018, https://doi.org/10.1016/j.jweia.2018.06.001

II. Urquhart M., Ljungskog E. and Sebben S., *Surrogate-based optimisation using adaptively scaled Radial Basis Functions.* In: Applied Soft Computing - The Official Journal of the World Federation on Soft Computing (WFSC), Volume 88, ISSN 1568-4946, 2020, https://doi.org/10.1016/j.asoc.2019.106050

III. Urquhart M., Varney M., Sebben S. and Passmore M., *Aerodynamic drag improvements on a square-back vehicle at yaw using a tapered cavity and asymmetric flaps.* In: International Journal of Heat and Fluid Flow, Volume 86, 2020, ISSN 0142-727X, 2020, https://doi.org/10.1016/j.ijheatfluidflow.2020.108737

IV. Urquhart M., Varney M., Sebben S. and Passmore M., *Drag reduction mechanisms on a generic square-back vehicle using an optimised yaw-insensitive base cavity.* Submitted to: Experiments in Fluids (2021-06-08)

V. Urquhart M., Sebben S. *Optimisation of trailing edge flaps on the base cavity of a vehicle for improved performance at yaw* Submitted to: Flow, Turbulence and Combustion (2021-09-09)

Division of work

I. All setup, simulation work and analysis for Paper I was done by Urquhart. The wind tunnel tests used for numerical validation were performed by Dr Sterken. Urquhart wrote the first manuscript which was discussed, reviewed and revised by all authors.

II. The fluid simulations and benchmarking of the surrogate model was performed by Urquhart. The package for scattered interpolation was created by Ljungskog with functionality added by Urquhart. The code for sampling plan creation, Proper Orthogonal Decomposition and surrogate model creation was written by Urquhart. Planning of the research project, discussion of the results and algorithmic improvements to the surrogate model was jointly performed by Urquhart and Ljungskog. Urquhart wrote the first manuscript which was discussed, reviewed and revised by all authors.

III. The tapered cavity geometry optimisation was done by Urquhart. The experimental plan was done by Urquhart and the experiments were performed by Urquhart and Varney. Urquhart and Varney wrote the first manuscript which was discussed, reviewed and revised by all authors.

IV. The tapered cavity geometry optimisation was done by Urquhart. The experiments were performed by Urquhart and Varney. Urquhart wrote the first manuscript which was discussed, reviewed and revised by all authors.

V. Urquhart designed the cavity and flap surfaces which were made into manufacturable parts by the consultancy firm AFRY. The servo control box and wireless communication was done by Volvo cars and modified by Urquhart for the control of flaps. Urquhart performed the experiments with help from Hobeika and Sterken. Urquhart wrote the first manuscript which was discussed, reviewed and revised by all authors.

Other relevant publications

I. Josefsson E, Hagvall R., Urquhart M., Sebben S., *Numerical Analysis of Aerodynamic Impact on Passenger Vehicles during Cornering.* In: SAE International, ISSN 0148-7191, 2018, https://doi.org/10.4271/2018-37-0014

Table of Contents

Abstract **i**

Acknowledgements **iii**

Nomenclature **iv**

Abbreviations **vi**

Thesis **vii**

Contents **x**

I Extended summary **1**

1 Introduction **3**
- 1.1 Project objective and limitations . . . 3
- 1.2 Outline . . . 4

2 Background **5**
- 2.1 Environmental aspect . . . 5
- 2.2 Vehicle testing procedures . . . 6
- 2.3 Real-world aerodynamics . . . 7
- 2.4 Wake aerodynamics . . . 10

3 Methodology **11**
- 3.1 Geometries . . . 11
  - 3.1.1 Generic model . . . 11
  - 3.1.2 Full-scale models . . . 12
- 3.2 Experimental methodology . . . 14
  - 3.2.1 Loughborough University Large Wind Tunnel . . . 15
  - 3.2.2 Volvo Cars Aerodynamic Wind Tunnel (PVT) . . . 17
- 3.3 Numerical methodology . . . 18
  - 3.3.1 Unsteady simulations . . . 19
  - 3.3.2 Steady-state simulations . . . 20

3.4 Optimisation 21

4 Cavities **25**

4.1 Cycle averaged drag optimised cavity 25

4.1.1 0 °-yaw 26

4.1.2 5 ° & 10 °-yaw 33

5 Cavities with trailing edge devices **39**

5.1 Trailing edge kick 39

5.1.1 0 °-yaw 39

5.1.2 5 °-yaw 42

5.2 Flaps on the Windsor body 44

5.2.1 0 °-yaw 44

5.2.2 5 ° & 10 °-yaw 45

5.3 Flaps on the XC40 51

5.3.1 0 °-yaw 51

5.3.2 5 ° & 10 °-yaw 53

5.4 Influence of wake balance at yaw 57

6 Concluding remarks **59**

6.1 Future work 60

7 Summary of papers **61**

7.1 Paper I 61

7.2 Paper II 61

7.3 Paper III 62

7.4 Paper IV 62

7.5 Paper V 63

Bibliography **71**

II Appended papers **73**

Paper I 75

Paper II 89

Paper III 109

Paper IV 125

Paper V 147

Part I

Extended summary

Chapter 1

Introduction[1]

This thesis is focused on passenger vehicle wake aerodynamics, specifically the relation between the base drag and crosswinds.

Personal transportation is a central part of modern society, enabling us to travel and freely move between places of work and our homes. The passenger car has had a central role in the development of personal transportation and continues to be the primary means of travel for many. However, it is clear that the energy consumption and environmental strain needs to be reduced.

Passenger vehicles were responsible for around 12 % of all greenhouse gas emission in Europe 2017 [2]. The targets for greenhouse gas emissions have become more strict globally. This is reflected in the rules and regulations as testing flexibilities have been identified as contributing factors to the increasing gap between certified energy consumption and that experienced by customers [3, 4]. Part of the identified gap was due to aerodynamically relevant factors such as tyre selection. Newer testing cycles have reduced these flexibilities while increasing the contribution of aerodynamics to the overall resistive force [5]. However, aerodynamically relevant factors from external disturbances, such as side wind, are not considered in the certification process of passenger vehicles today.

Road vehicles are characterised by massively separated wakes dominated by pressure drag. To reduce the pressure drag, attention has mainly been focused on improving the pressure recovery in the base wake to reduce the pressure difference between the front and rear of the vehicle. Vehicle modifications are typically investigated in idealised conditions without side wind, and there is comparatively little information available in the literature on the complete wake flow at yaw.

1.1 Project objective and limitations

From the literature it is known that vehicles with similar aerodynamic performance can have largely differing sensitivity to wind. The objective of this thesis is to increase the knowledge of the wake structures at yaw and their relation to the vehicle's base pressure. Thus, different geometric modifications to the base of vehicles are studied at moderate yaw angles.

---

[1] Parts of this thesis have been carried over from the Licentiate thesis [1]

Optimisation is central in this work to create reference geometries with reduced sensitivity to side wind. This helps to facilitate the project goal of understanding the coupling between the wake topology at yaw and vehicle drag.

Many factors are related to real-world operating conditions that can influence vehicle aerodynamics. In this work, it is only steady side wind that is considered.

1.2 Outline

The first part of this thesis provides the context for this work. This is followed by a background in vehicle aerodynamics. Further, the methodology used in the included papers is presented. After the methodology chapter, two chapters with results and discussion are presented. These are on base cavities and base cavities with trailing edge modification respectively. Finally, some concluding remarks and possible future work is presented, ending with a summary of the appended papers.

Chapter 2

Background

The environmental aspects of passenger vehicles as well as the aerodynamically relevant factors of real-world operating conditions are introduced in this chapter.

2.1 Environmental aspect

Greenhouse gas (GHG) emissions and other environmental concerns, such as urban air quality, are driving factors in passenger vehicle emission legislation. The transport sector was responsible for 27 % of the total greenhouse gas emissions in the EU (CO_2 equivalent) year 2017, including international aviation and maritime emissions [2]. Passenger cars were the largest contributors of GHG emissions in the transport sector, responsible for 44 % of the sectors total emissions, Figure 2.1. This means that passenger vehicles emitted more than 10 % of all GHG emissions in the EU year 2017, which is more than three times that of aviation. This is reflected in the regulations with historically tightening emission targets and proposed future reductions, seen in Figure 2.2 [6]. Each country is compared in terms of gCO_2/km normalised to the New European Driving Cycle (NEDC) cycle. Standardised driving cycles are used as a tool by governing bodies to quantify the vehicle's performance and enable comparison between different vehicles and manufacturers. These performance figures can also be used by consumers to compare the range or fuel consumption between vehicles from different manufacturers.

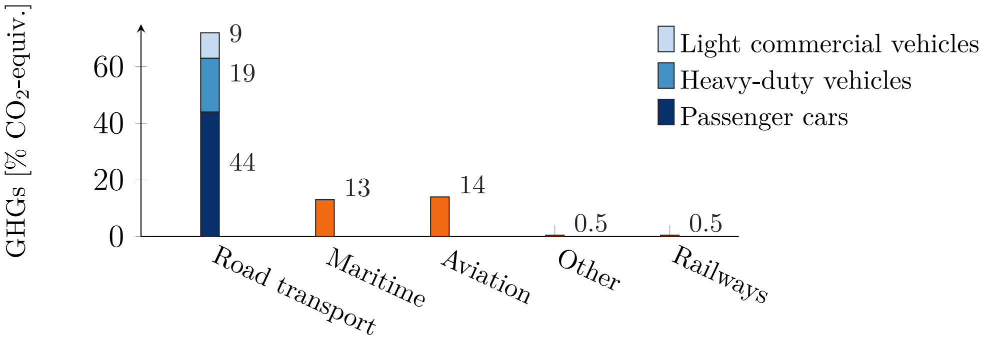

Figure 2.1: *Greenhouse gas emissions within the transportation sector 2017. Data from the European Environment Agency [2].*

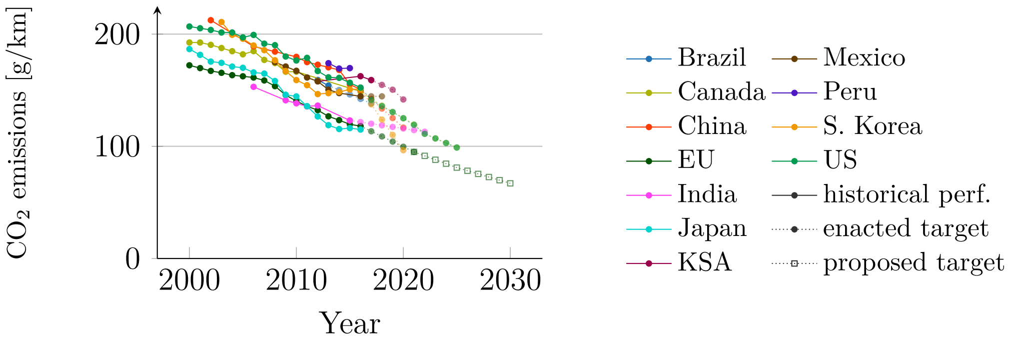

Figure 2.2: *Historical fleet CO$_2$ regulations and current standards normalised to the NEDC cycle for passenger cars, data from The International Council on Clean Transportation [6].*

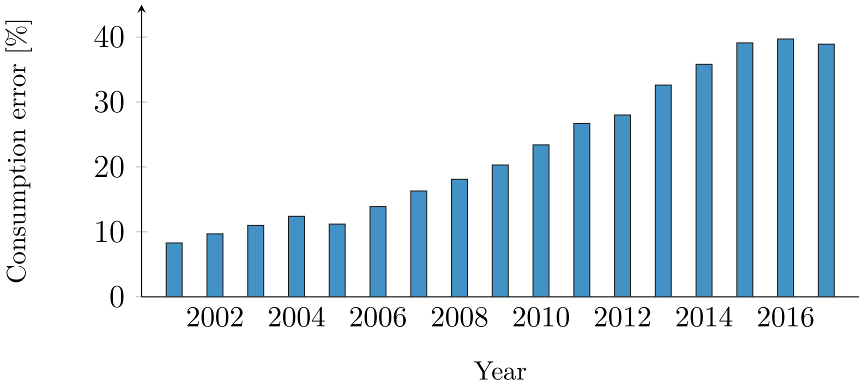

Figure 2.3: *Real-world fuel consumption increase as a percentage of the manufacturer stated fuel consumption using the NEDC testing cycle. Data from the report by the ICCT [7].*

2.2 Vehicle testing procedures

Targeted emission levels have been decreasing historically. Meanwhile, the difference between the certified fuel consumption and that reported by consumers has increased. Tietge et al. [7] compiled data from 15 different sources in eight countries containing 1.3 million vehicles showing how the gap has been increasing as can be seen in Figure 2.3. During this period the advertised fuel consumption reduced by approximately 30 %, but due to the growing gap the real-world consumption only reduced by 10 % [7]. Testing flexibilities have increasingly been exploited and the vehicles have been optimised for non-representative operating conditions [3, 4]. By 2015 the discrepancy reached 39 %, diminishing the effectiveness of legislation and reducing customer satisfaction. A quarter of the difference in 2014 was determined to be due to road load determination, where tyre selection, vehicle preparation, and ambient test conditions were influencing factors [4]. Yang et al. [6] stated that the growing gap is a concern, undermining the legitimacy of using standardised testing.

To address this issue, the European Council has implemented a new testing

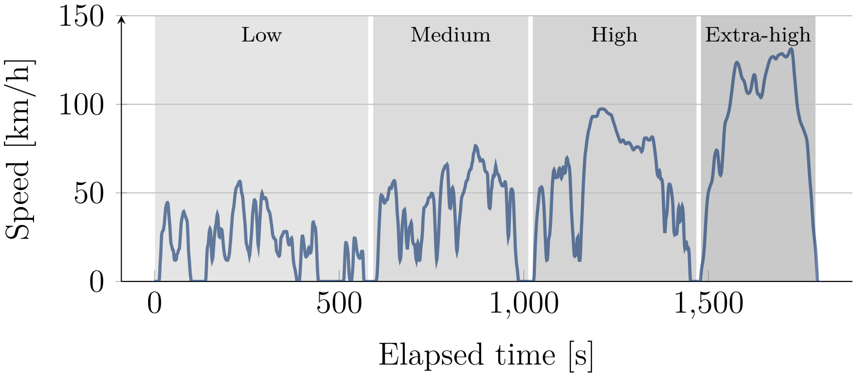

Figure 2.4: *WLTC Class 3 driving cycle.*

procedure as of 2017 called the Worldwide Harmonised Light vehicle Test Procedure (WLTP). The WLTP aims to reduce the divergence between real-world and advertised fuel consumption performance by reducing some of the testing flexibilities and incorporating new driving cycles which are more representative of real-world use cases. The Worldwide Harmonized Light vehicle Test Cycle (WLTC), relevant for the most commonly sold passenger vehicles, is illustrated in Figure 2.4.

The WLTC is split into four phases, Low, Medium, High, and Extra-high with several acceleration and braking zones. Aerodynamics has become more important in the WLTC, compared to the NEDC, with an increased average speed, from 34 km/h to 46 km/h, and an increased maximum velocity from 120 km/h to 131.3 km/h.

In a study by Pavlovic et al. [5], 20 petrol vehicles were tested using both the WLTC and the NEDC testing cycles. For an average performing vehicle in the high test mass and high road load category, the aerodynamic forces were responsible for 27.6 % of the traction energy required in the WLTC and 23.0 % in the NEDC. This highlights the increased importance of aerodynamics in the more representative WLTC.

2.3 Real-world aerodynamics

The aerodynamic drag is part of the overall driving resistive force, $F_{\text{resistive}}$. The overall resistive force can be split into the force required to accelerate the vehicle, the force due to road incline, the rolling resistance and the aerodynamic drag [8] as,

$$F_{\text{resistive}} = ma + mg \sin\theta_{\text{incline}} + F_{\text{RR}} + F_{\text{D}}. \tag{2.1}$$

Aerodynamic forces are often normalised by the freestream dynamic pressure and the vehicle's frontal area, e.g. the drag coefficient, C_{D}, becomes

$$C_{\text{D}} = \frac{F_{\text{D}}}{\frac{1}{2}\rho_\infty V_\infty^2 A} \tag{2.2}$$

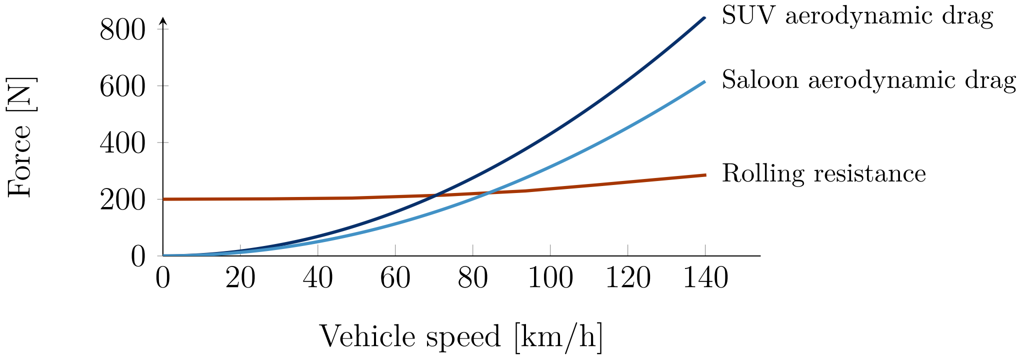

Figure 2.5: *Rolling resistance and aerodynamic drag of a representative SUV and saloon type vehicle. Rolling resistance from [9]. The area and drag for the SUV and saloon were calculated using the mean area and drag coefficient of the vehicles presented in [10] and [11]. Saloon mean* $C_D = 0.304$*, mean* $A = 2.259$ *and SUV mean* $C_D = 0.358$*, mean* $A = 2.626$*.*

where A is the model's projected frontal area (m^2), ρ_∞ is the air density (kg/m^3) and V_∞ is the freestream velocity (m/s). The lift coefficient, C_L, is normalised the same way as the drag coefficient, Equation 2.2, but acting in the vertical direction. The subscripts, FL and RL, denote front lift and rear lift respectively where the lift force is split into two components acting at the wheels. Moment coefficients are calculated similarly but normalised by the length of the vehicle's wheelbase.

There is a square relationship between the aerodynamic force and the velocity, the effects of which are shown in Figure 2.5. On a flat road at a constant velocity, the aerodynamic drag becomes the dominant resistive force above approximately 70-80 km/h depending on the vehicle. The drag on the vehicle is comprised of pressure and shear forces. Road vehicles are short blunt bodies characterised by massively separated wakes where 90 % of the total drag is pressure drag [12].

During vehicle development, it is typical to use a combination of low turbulence wind tunnel testing and numerical simulations under constant wind conditions with fixed vehicle position. The value of the drag coefficient, C_D, is then used as a constant figure for the evaluation of the aerodynamic performance of the vehicle. This is a simplification from real-world conditions where several commonly occurring factors that influence aerodynamics and the value of C_D exists. Examples of such factors are wind, turbulence, cornering, ride height, traffic and tyre pressures.

Gargoloff et al. [13] investigated the combined effect of on-road turbulence intensity and yaw angle, or side wind. The results show synergy effects between the on-road turbulence intensity and the side wind angle. However, the side wind angle was found to be the dominant drag increasing factor.

In a study of 51 passenger vehicles of different vehicle types, Windsor [10] evaluated the sensitivity of each vehicle to yawed flow and found that the drag sensitivity to yaw tended to increase as drag decreased for saloon and sports type vehicles. This indicates that the current methods of optimising vehicles in idealised

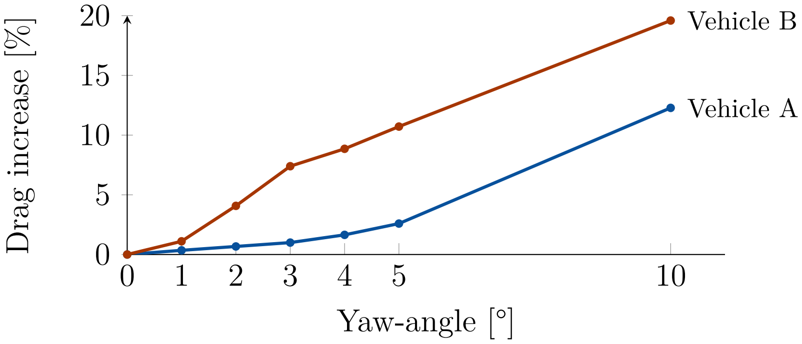

Figure 2.6: *Drag increase per yaw angle for two saloon vehicles. Data from the study by Windsor [10].*

conditions most likely contributes to the increased gap between the certified and real-world performance. Two of the vehicles from the study by Windsor [10] are shown in Figure 2.6 where vehicle B is more sensitive to side wind. Both vehicles are of saloon type, however, comparing vehicle A and B without considering the performance over the entire operating range can result in an unrepresentative performance figure.

Howell et al. [14] developed the cycle-averaged drag coefficient, C_{DWC}, which takes into account the wind distribution and the vehicle's speed across the entire driving cycle to create a more representative aerodynamic performance figure. THey calculated the cycle-averaged drag coefficient for 28 vehicles using the WLTC and found that the typical increase between the drag coefficient at 0°-yaw and C_{DWC} to be 5 %, with the smallest and largest increase being 2.2 % and 11.4 %, respectively. In their work, a simplified estimate of the cycle averaged drag was created by incorporating four weighted drag values at different yaw angles that can be used as an engineering tool during vehicle development. It was stated that the relative weighting of the terms was found through regression and carries no physical meaning, nor does the weighting add up to 1.

Varney et al. [15] used the cycle-averaged drag proposed by Howell et al. [14] to study asymmetric side tapering. The equation was modified by dropping the 15°-yaw term due to its relatively small contribution as

$$C_{\mathrm{DWC}} = 0.53C_{\mathrm{D0}} + 0.345C_{\mathrm{D5}} + 0.13C_{\mathrm{D10}} \tag{2.3}$$

where the subscript denotes the yaw angle. The C_{DWC} variant using the modification by Varney et al. [15] has been used here to optimise vehicle geometry.

It is clear from the literature that evaluating the vehicle's aerodynamic performance in idealised conditions is a large simplification. The heavy vehicle industry has recognised this and employs wind-averaged drag values to a larger extent during development. The passenger vehicle industry has also begun to realise the potential benefits from more active elements such as reducing ride height at high speeds or partially closing off cooling when permissible to improve overall efficiency.

In the author's opinion, we will see a continued increase in innovation where more of the aerodynamically influencing aspects of the driving conditions, like side wind, are considered during development.

2.4 Wake aerodynamics

Different wake characteristics, both qualitative and quantitative, have been used to study their size, shape, spectral information, modal information, closure point location, kinetic energy, turbulent kinetic energy, recirculation angles, and vorticity distribution [16–19]. Vehicle wakes are unsteady and it is of interest to map both the time-averaged results as well as the unsteady behaviour. Most studies are performed without considering yaw. Due to the highly 3-dimensional nature of the wake, especially at yaw, it is important to study the full wake.

There are several ways to improve the wake flow and reduce drag. These methods all aim to alter the flow in some way, improving wake balance, reducing wake size, etc. One of the commonly used methods to improve vehicle drag is to apply a rearward-facing cavity. This is an effective method of reducing drag at 0°-yaw with improvements in the range of 10 % [20–22].

Tapering of the rear of the vehicle is also an effective drag reduction technique, with reductions of up to 20 % [15, 23]. It has also been shown that the combination of tapering and a cavity results in further improvements in drag than either of the methods separately [24].

Changes to the geometry often result in several aspects of the wake changing simultaneously, making it difficult to separate and pinpoint the drag-reducing mechanisms of the complete wake. Perry [25] found that a wake where the impingement was located close to the centre of the base had low drag when varying the rear top and bottom taper of a simplified vehicle. However, the wake closure point, size and the kinetic energy within the wake showed no clear trend in relation to drag. Additionally, the added rearward-facing tapered surfaces also contribute to drag, requiring a trade-off between the surfaces with attached flow and the surfaces in separated flow [23].

In this work, both numerical simulations and experiments with measured pressures and flow fields are used to investigate the wake characteristics, particularly at yaw. This is done for simplified model scale geometries as well as full-scale detailed vehicles. The work is focused on different rear end extensions where tapering and cavities are combined. Further different trailing edge modifications are applied to the cavities to improve drag for different yaw angles.

Chapter 3

Methodology

An overview of the methodology used in the included papers is described here.

3.1 Geometries

Three vehicles were used in this thesis, one generic model and two full-scale detailed models.

3.1.1 Generic model

The generic 25 % model is a modified version of the Windsor body which has been modified by Pavia et al. [26] to include wheels, as shown in Figure 3.1a. Figure 3.1b shows the pressure tap locations on the base.

The model was tested with two different cavities, a straight cavity, Figure 3.2a, and a tapered cavity, Figure 3.2b. The cavity is 50 mm deep, corresponding to 5 % of the vehicle length. The angles of the tapered cavity were optimised using numerical simulations to reduce the cycle averaged drag and will be further explained in Chapter 4. A variant where the tapered cavity is filled was also tested to assess the effect of tapering alone.

The tapered cavity was also tested with nine unique trailing edge flaps that each can take on the angles 0°, 7°, 14° or 21°. A positive angle denotes the flap moving from the centre outward. The flaps are 20 mm long, corresponding to 2 % of the vehicle length, Figure 3.3. The diffuser was not equipped with flaps to simplify the

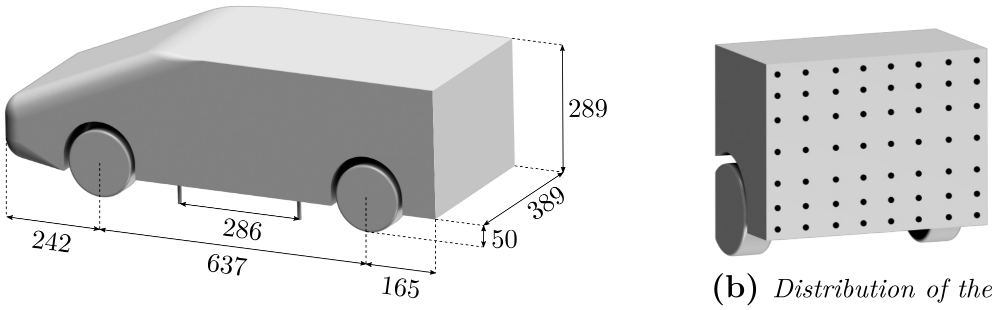

(a) *Windsor geometry.*

(b) *Distribution of the 7×8 wall static pressure measurement locations.*

Figure 3.1: *Windsor geometry with wheels. Measurements are given in* mm.

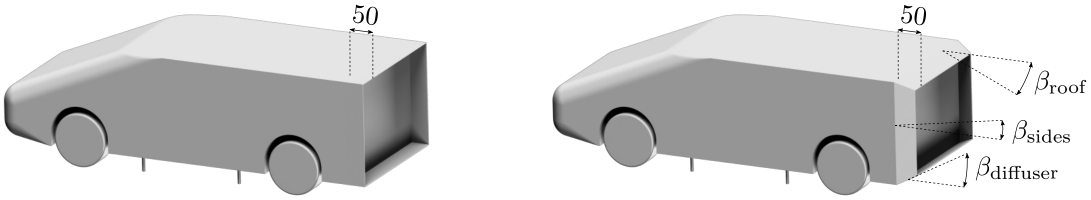

(a) *Straight cavity.* **(b)** *Tapered cavity.*

Figure 3.2: *Windsor geometry with wheels. Measurements are given in* mm.

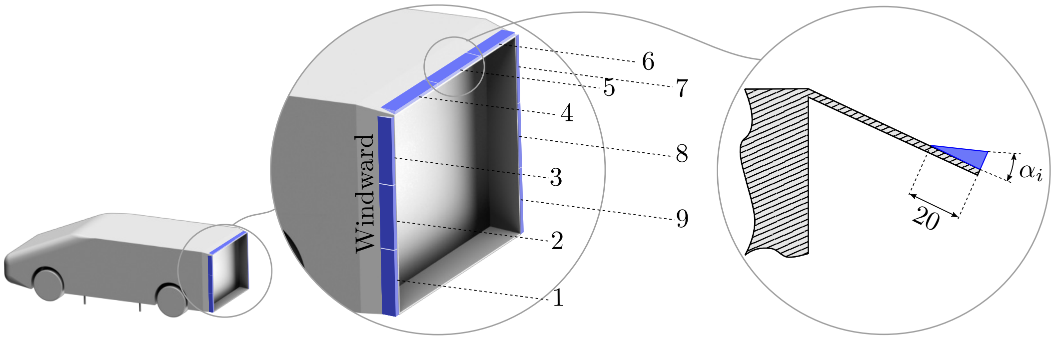

Figure 3.3: *Cavity with flap naming convention. Measurements in [mm].*

tests due to the limited ground clearance. Each flap has locating pins to ensure correct placement when manually changing them between tests.

3.1.2 Full-scale models

Two full-scale vehicles were used here. A Volvo XC60 AWD featuring closed cooling and additional underbody panels as described by Sterken et al. [27–29] to improve flow to the rear. The vehicle is equipped with an additional tapered 3/4 extension at the edges of the base covering the roof and sides, creating a 3/4 cavity, Figure 3.4a.

The taper adds 5° of additional tapering, compared to the original geometry,

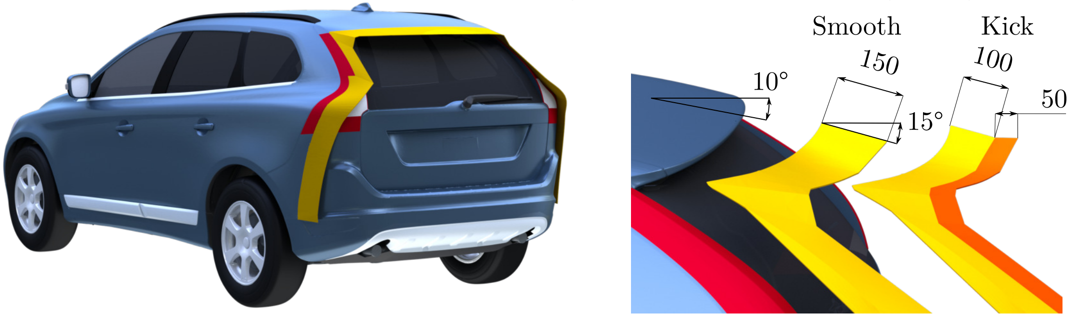

(a) *Rear view of the Volvo XC60 with a tapered 3/4 cavity.* **(b)** *Cavity, measurements in [mm]. Taper angle referenced to the horizon.*

Figure 3.4: *Volvo XC60 AWD geometry.*

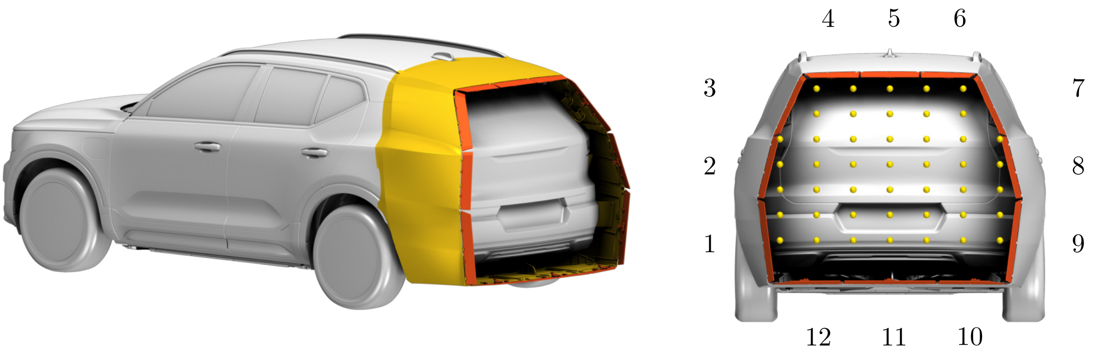

(a) *Cavity and flaps on the Volvo XC40 recharge.*

(b) *45 pressure probe locations and the flap naming convention.*

Figure 3.5: *Volvo XC40 recharge geometry.*

making the total taper angle approximately 15°. The extensions are 150 mm long which is approximately 3 % of the vehicle length. One of the variants investigated is the $^{3}/_{4}$ cavity where the trailing edge is angled outward by 15° relative to the cavity tapering to counteract the tapering angle, shown in Figure 3.4b.

The second full-scale model is a Volvo XC40 recharge electric vehicle fitted with an approximately 150-200 mm deep cavity, or 5 % of the vehicle length, with twelve additional 80 mm long flaps, or 2 % of the vehicle length, extending the cavity, Figure 3.5a. The cooling is closed and the rearview mirrors have been removed. The rims are covered and the bottom of the cavity is on the same height as the flat floor to improve the flow to the rear of the vehicle. The cavity is tapered similar to the XC60 with approximately 15° tapering on the sides and roof with no tapering on the bottom. Figure 3.5b shows the pressure tap locations on the base and the flap naming convention.

The flaps can move ±25° relative to the existing tapering. The flaps were controlled using Dynamixel XL430-W250-T servos connected with linkages and horns with a 1:1 ratio between the movement of the flap and the servo. The servos have a stall torque of 1.4 Nm. The system was controlled using an Arduino Mega with a Dynamixel shield connected to the servos. The flap angles were set wirelessly from the control room outside of the test section using an Xbee PRO S1. The wireless control allows for several designs to be tested with a short turnaround while the tunnel is running continuously. For each tested design, the position of the servo horns was verified ($<\pm3°$) before sampling the design performance. The cavity and flaps, as tested in the wind tunnel, can be seen in Figure 3.6.

The evaluation of a design takes approximately 1 min and 30 seconds. First, the flaps are all set to the −25° degree position. This is expected to cause the flow to separate over the flaps as the total angle is approximately 40° relative to the freestream flow. This is done to reduce any hysteresis effects where the current design performance is dependent on the previous design tested. After 10 seconds, the flaps are all set to the desired position. Once the flaps are in position the flow is allowed to develop for 10 seconds, then a 20 second average is taken.

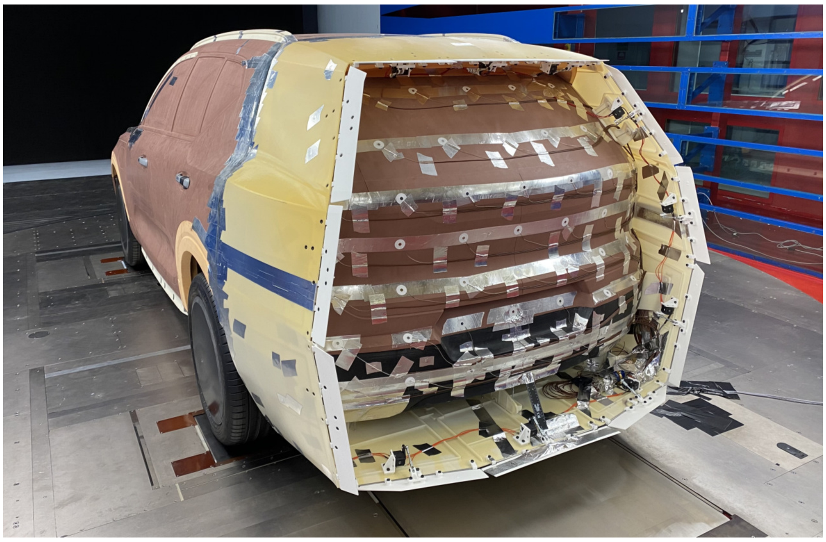

Figure 3.6: *Volvo XC40 cavity.*

Even though the evaluation of one design is relatively fast it is not possible to test all design combinations. Limiting the 12 flaps to 5 angles per flap (-25.0,-12.5, 0.0, 12.5, 25.0), it would take roughly 700 years to test all designs. In this work, each angle was limited in 2° increments, it would take approximately 300 billion years to test all possible configurations for one yaw angle. This highlights the need for efficient optimisation methods to take advantage of the large design space. The flaps were limited to 2° increments to reduce excessive testing of similar designs, increasing exploration of the design space.

The repeatability was evaluated by testing the same design 20 times following the mentioned procedure where the flaps are first set to the $-25°$ degree position before testing the configuration. By comparing the disturbance in the force to the mean of the 20 tests, the repeatability for a 95 % confidence interval was calculated as $\pm C_{\mathrm{D}} = 0.0008$ at 0°-yaw.

3.2 Experimental methodology

A positive yaw angle is denoted with the nose pointing right following the SAE standard for yaw J1594 [30]. In the presented results, the wind moves from left to right in the vehicle's driving direction when the model is yawed. The coordinate system is shown in Figure 3.7, where the roll, pitch, and yaw moments act along the x, y, and z-direction using the right-hand rule and Θ denotes the yaw angle. The coordinate system remains the same for all vehicles.

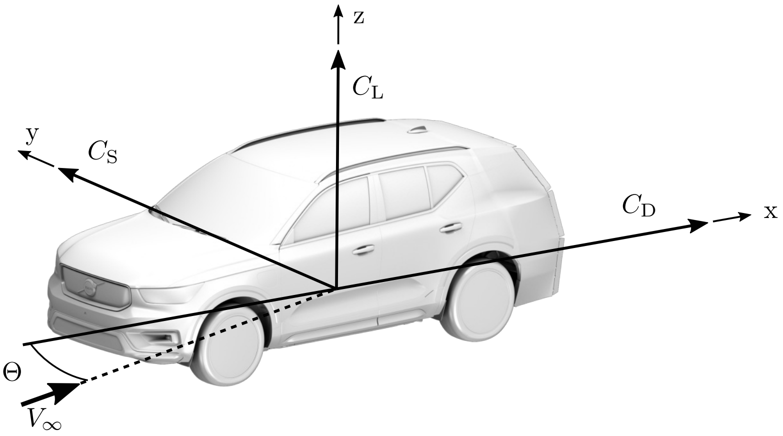

Figure 3.7: *Vehicle coordinate system.*

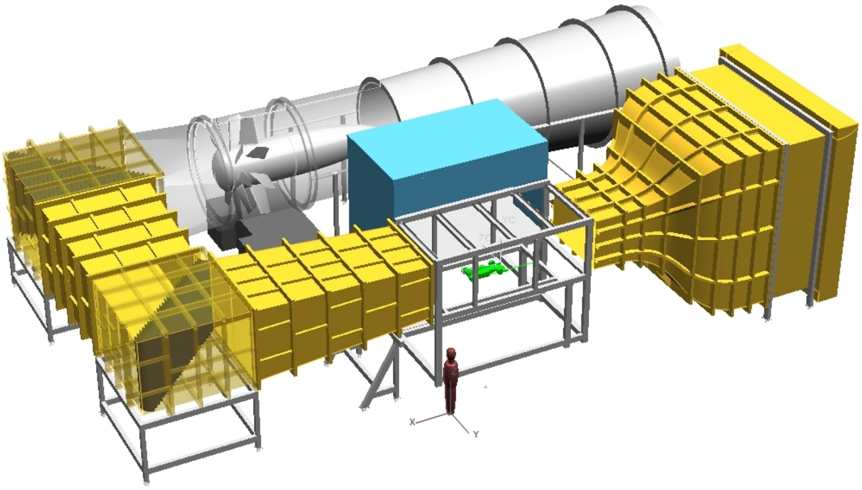

Figure 3.8: *The Loughborough University Large Wind Tunnel Johl [31].*

3.2.1 Loughborough University Large Wind Tunnel

The wind tunnel tests were performed in the Loughborough University Large Wind Tunnel, Figure 3.8, which is an open return, closed test section facility. The rectangular working section is 1.92 m×1.3 m with 0.2 m corner fillets and is 3.6 m long. The tunnel is capable of speeds up to 45 m/s. The tests were run at 40 m/s resulting in a Reynolds number of $Re_{\sqrt{A}} = 9.6 \times 10^5$ based on the square root of the vehicle frontal area.

The model is mounted to the six-component balance with four 8 mm pins which are located between the wheels to reduce the impact on the overall flow. The balance data was sampled at 300 Hz and averaged for 300 s. The wheels are stationary and tangent to the wind tunnel floor which has debossed floor pads to prevent grounding. More information on the wind tunnel can be found in [31].

Only negative yaw angles were tested experimentally to avoid obscuring part of the wake from the cameras when performing Particle Image Velocimetry (PIV). Due to this, all results are mirrored to reflect a positive yaw angle with the nose pointing right following the SAE standard J1594 [30]. For all presented results in this thesis, the wind moves from left to right in the vehicle driving direction when the model is yawed.

The repeatability between tests was estimated by running the same configuration at 0°, 5°, and 10°-yaw on different days, resulting in a total of 7 unique samples. From these samples, the 95 % C_D confidence interval was calculated to by ±0.001 at 0°-yaw, ±0.002 at 5°-yaw and ±0.0025 at 10°-yaw.

The surface static pressure measurements were recorded for 300 s at 260 Hz using a 64 channel differential pressure scanner. A time correction is applied to the data which time-aligns each of the 64 channels [32].

The base drag, C_DB, is calculated using the pressure from each tap as well as an incremental area associated with each tap. Similarly, the moment on the base, (C_MB), is calculated by adding the contribution from each pressure measurement around the centre of the base. The lateral and vertical base moment is normalised by the width and the height of the base respectively.

Two-point correlation is used to evaluate the temporal correlation of one base pressure tap to all of the pressure taps on the base. The two-point correlation for a flow variable, ξ, and two of the pressure taps, is defined as

$$C_\xi(x_A, x_B) = \overline{\boldsymbol{\xi}'(x_A)\boldsymbol{\xi}'(x_B)} \tag{3.1}$$

where x_A and x_B are the spatial coordinates of interest and $\boldsymbol{\xi}'$ is a vector of the fluctuating flow variable ξ. The correlation is large and positive for two correlated signals in phase, large and negative for two correlated signals 180° out of phase and small for uncorrelated signals. A variant of the correlation is also used which is normalised by the product of the RMS of each correlated signal resulting in a self correlated signal becoming 1.

The wake flow field was captured using tomographic Particle Image Velocimetry (PIV) and processed using commercially available hardware and software (DaVis® 8.4) from LaVision®. 1000 image pairs were taken for each measurement at a frequency of 5 Hz, resulting in 200 s of data.

Four cameras were used to capture the measurement volume, shown in Figure 3.9. The flow was seeded using three rakes, Figure 3.9b, each producing 400,000 bubbles per second. The particles were Helium Filled Soap Bubbles (HFSB) which were around 300 µm in diameter and illuminated with a 200 mJ Nd:YAG double-pulse laser from Litron® through a volume optic to distributed the beam over the required measurement volume of interest.

The seeding density is not sufficient for high-quality PIV data at 40 m/s and was instead run at 30 m/s. This is above the requirement for a Reynolds insensitive flow field for this specific model [33] while maintaining a sufficient particle seeding density to reduce the reconstruction error [34]. The force and base pressure measurements were conducted at 40 m/s to utilize more of the available resolution from the balance and pressure measurement systems.

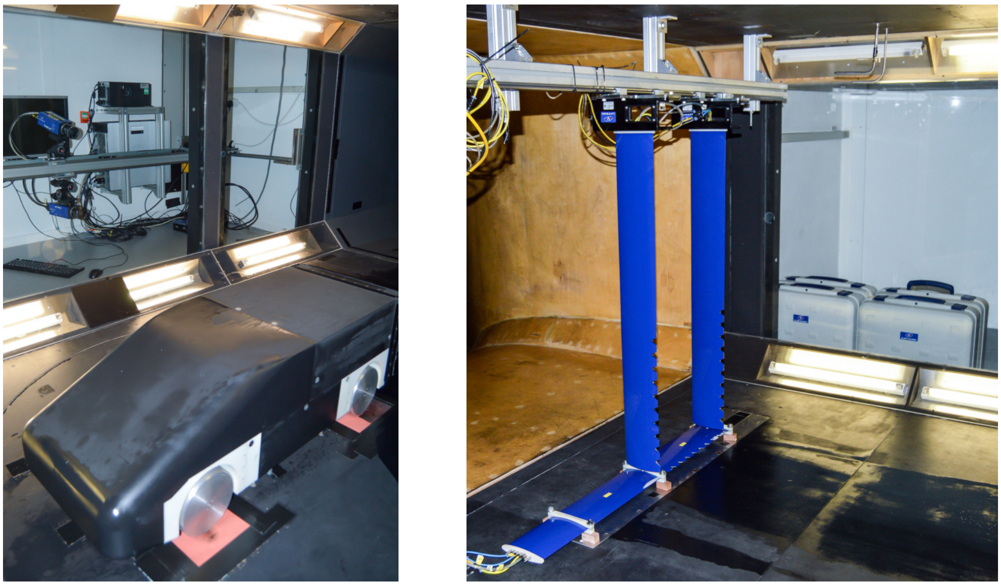

(a) *Camera position and orientation relative to the model.* **(b)** *Seeding setup.*

Figure 3.9: *Tomographic PIV setup in the working section.*

3.2.2 Volvo Cars Aerodynamic Wind Tunnel (PVT)

The full-scale wind tunnel experiments were performed at the Volvo Cars Aerodynamic Wind Tunnel (PVT) capable of speeds of up to 250 km/h. In this work, the full-scale tests were done at 100 km/h (27.78 m/s) resulting in a Reynolds number of $Re_{\sqrt{\mathrm{A}}} = 3.1 \times 10^6$ based on the square root of the vehicle frontal area, A. The tunnel is of closed return type with slotted walls, an overview is given in Figure 3.10. The test section is 27 m^2 resulting in a blockage ratio of approximately 10 % for full-scale geometry.

The tunnel is equipped with a five belt moving ground system mounted on a turntable to allow yawing of the vehicle. There is a boundary layer control system consisting of a scoop followed by distributed suction as well as tangential blowers behind each belt, extending their apparent length to replicate on road conditions. The vehicle is connected to a six-component balance using four struts which fixate the vehicle's position and height.

Forces and moments are measured by the six-component balance and are non-dimensionalized to coefficients that are corrected for blockage effects. The reported repeatability within the same test is $C_\mathrm{D} = \pm 0.001$ and the tunnel is accredited according to the European Accreditation procedure EA 4/02 [35]. The repeatability for the flap movement was calculated to $C_\mathrm{D} = \pm 0.0008$ as was mentioned earlier.

Base pressures were taken using a PSI ESP-64HD 64 channel pressure scanner where each measurement was averaged for 20 s. A traversing unit was used to capture wake planes featuring two 12-hole pressure probes, or omniprobes, mounted 56 mm apart vertically and were swept with a 112 mm vertical spacing. The probes

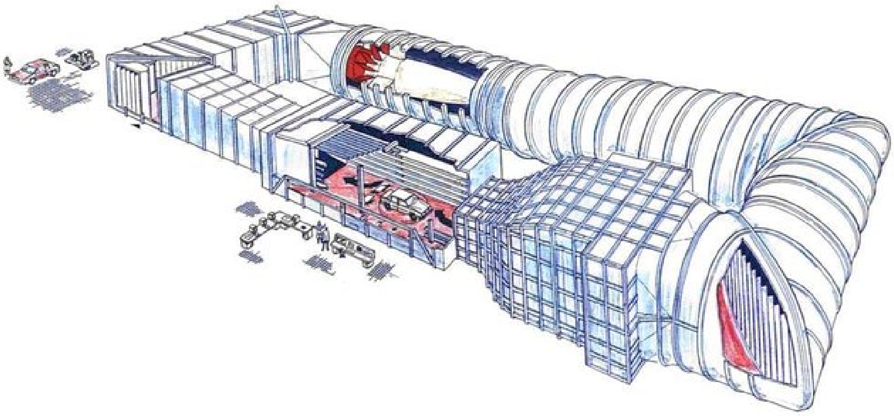

Figure 3.10: *Volvo Cars Aerodynamic Wind Tunnel (PVT).*

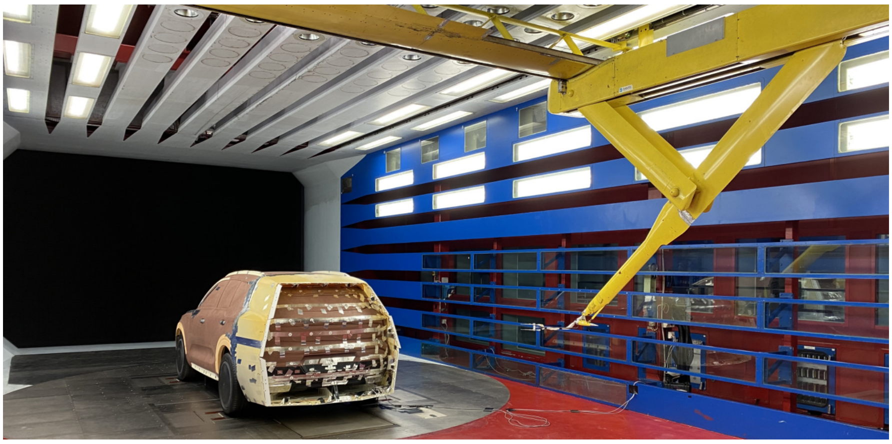

Figure 3.11: *Volvo wind tunnel experimental setup with traversing unit for wake measurements.*

are capable of capturing flow within ±150° [36]. The probes were placed at a 45° angle to better capture the reversing flow in the wake. The mounted vehicle along with the traversing unit is shown in Figure 3.11. More information on the wind tunnel can be found in [35, 37].

3.3 Numerical methodology

The numerical simulations were performed using the commercial Finite Volume Method Computational Fluid Dynamics (CFD) solver Star-CCM+. The mesh was refined in areas with large gradients such as the wake and around the wheels. Approximately 12 prism layers were used on all external surfaces to achieve a $y^+ < 1$ and an acceptable growth ratio of 1.6 [38]. The resulting hexahedral dominant mesh consisted of approximately 130×10^6 cells for full-scale geometry and 90×10^6 cells for ¼-scale geometry. A 2$^{\text{nd}}$-order accurate spatial discretisation scheme was used where the gradients were computed using a hybrid Gauss-Least Squares method.

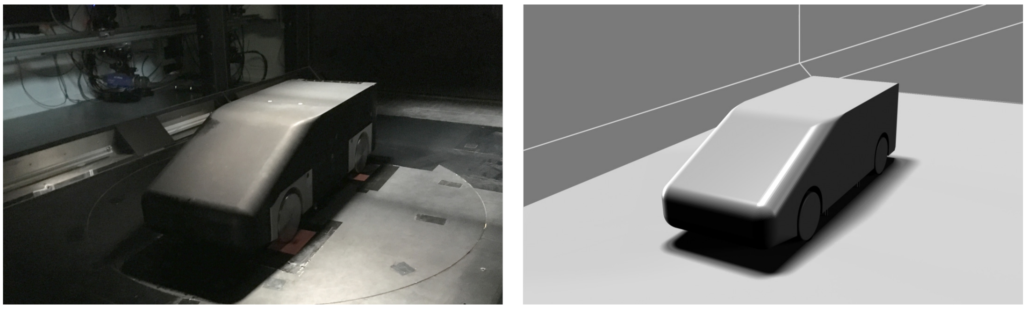

Figure 3.12: *The Loughborough University Large Wind Tunnel, left physical tunnel, right simulated domain.*

The full-scale simulations were run using a large domain to model open road conditions. The model-scale simulations were performed with a domain replicating the physical Loughborough University Large Wind Tunnel, Figure 3.12. The full-scale geometry was run using a time-resolved unsteady method while the model-scale geometry was run using both steady-state and unsteady simulations.

3.3.1 Unsteady simulations

The unsteady simulations were run using a hybrid RANS - Large Eddy Simulation (LES) approach, two-equation Improved Delayed Detached Eddy Simulation (IDDES) SST k-ω.

The timestep for the unsteady full-scale simulations was $2.5 \times 10^{-4} s$, with 7 inner iterations, which gives an average convective Courant number of 0.9, with more than 70% of the cells being below 1. The Courant number for a cell is defined as $C_{\mathrm{Courant}} = |V|\Delta t/\sqrt[3]{v_{\mathrm{cell}}}$, where Δt and v_{cell} is the timestep and cell volume respectively. A 2.5 times smaller timestep was tested in the full-scale simulations showing less than 0.001 ΔC_{D}, or a 0.3 % difference in drag between the longer and shorter timesteps. The flow field and forces were averaged for 3 s which is more than 18 convective flow units ($t * V_{\infty}/L$) where L is the vehicle length. Transient data was captured for 12 s for some configurations to allow for time-resolved analysis of the flow field as low-frequency events around 1 to 2 Hz or a Strouhal number, $St \approx 0.1$, were expected based on test results from [29], where $St = f\sqrt{A}/V_{\infty}$. The timestep and averaging times are consistent with the findings by Ekman et al. [39] and is also a good compromise between accuracy and simulation cost.

Unsteady simulations of the ¼-scale geometry were also made to study the prediction accuracy using a higher fidelity simulation method. The timestep and averaging time were adjusted to $2.0 \times 10^{-4} s$ with an averaging time of 2 s after reaching fully developed flow.

The mesh resolution for the full-scale unsteady simulations was evaluated using two-point correlation. According to Davidson [40], the energy spectra, as well as the resolved turbulent kinetic energy ratio, are poor measures of LES resolution. A better alternative was found to be two-point correlation, where the number of

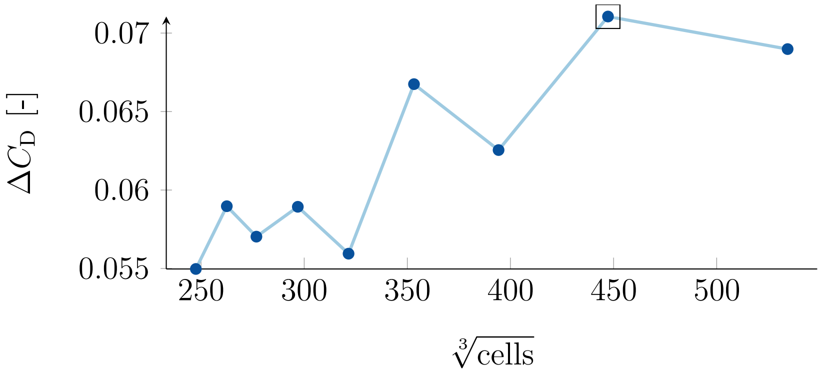

Figure 3.13: *Mesh study of the square-back geometry where ΔC_D is the difference in drag between simulations performed at 0°- and 10°-yaw. The selected mesh is marked with a square.*

correlated cells indicates the mesh resolution. Davidson [40] concluded that coarse LES preferably contained more than eight correlated cells, which was fulfilled in this work for all of the twenty investigated points.

With this numerical setup, the predicted drag change between configurations is on average within $\pm 0.001 C_\mathrm{D}$ of experiments for the full-scale unsteady simulations, with the sign of the predicted trend matching experiments for each configuration. The experimental data is taken from [28].

3.3.2 Steady-state simulations

The steady-state simulation were run using a Reynolds Averaged Navier Stokes (RANS), two-equation SST k-ω turbulence model. The steady-state simulations were only used at model-scale. Figure 3.13 shows the mesh study for the steady simulation method of the Windsor square-back model ranging from 15×10^6 to 150×10^6 cells. The predicted drag increase between 10°- and 0°-yaw is shown. The drag increase is compared to the cube root of the number of cells, as this is closely linked to the edge length of each cell in a hexahedral mesh, which is related to the spatial discretisation accuracy. The increasing trend in the drag delta is due to the drag prediction at 10°-yaw increasing as the cell count is increased while the changes at 0°-yaw are small. This is believed to be a result of the unsteady nature of the problem which is particularly prevalent at yaw. The mesh with approximately 90×10^6, the second finest mesh tested here, was selected as a compromise between simulation accuracy and the number of affordable optimisation iterations.

The method was approximately an order of magnitude more expensive compared to the steady-state simulation. Figure 3.14 shows the different simulation methods compared to wind tunnel experiments.

The prediction in both the trend and the absolute values improve with the unsteady method, which is an expected result due to the large separated wake. The absolute prediction difference is larger than expected compared to the full-scale

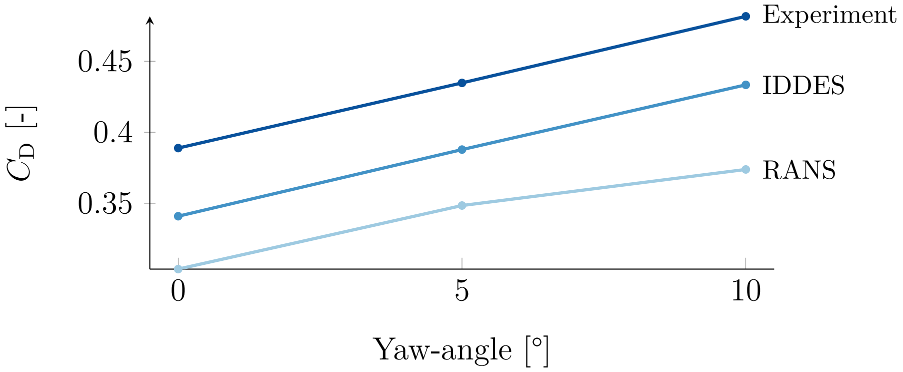

Figure 3.14: *RANS, IDDES and wind tunnel test results of the square-back geometry.*

testing. These differences are thought to be due to geometric factors that were not considered such as leakages, gaps in the model, surface roughness and mounting hardware which can be exaggerated at mode-scale.

3.4 Optimisation

In Paper II an optimisation algorithm was developed for use with expensive cost functions. Aerodynamic optimisation is often very costly as both numerical simulations or physical tests require significant resources. To solve this, a surrogate model-based algorithm was developed which is particularly beneficial when the number of achievable function evaluations is small.

The surrogate model is built from an initial set of designs which are decided using a Latin Hypercube (LHC). The Latin Hypercube sampling plan divides each design parameter into equally sized intervals where the same value for a given design parameter only occurs once. The distance between each sample is optimised to reduce clustering and increase the coverage within the sampling plan. The sampling plan optimisation algorithm is based on the work by J. Bates et al. [41]. Figure 3.15 shows an example of an optimised plan with 100 points in two design dimensions.

The surrogate model developed in this work is based on Radial Basis Function (RBF) interpolation. The RBF interpolant is analogous to a neural network with a single layer. The basis function combines the inputs linearly as

$$u(\mathbf{x}) = \sum_{i=1}^{N} w_i \xi_i(\|\mathbf{x} - \mathbf{x_i}\|_2) \tag{3.2}$$

where w_i are the weights, ξ_i is the Radial Basis Function, N is the number of sampled designs and $\|\mathbf{x}-\mathbf{x_i}\|_2$ denotes the Euclidean distance between the evaluated design $\mathbf{x}$ and the i-th design $\mathbf{x_i}$.

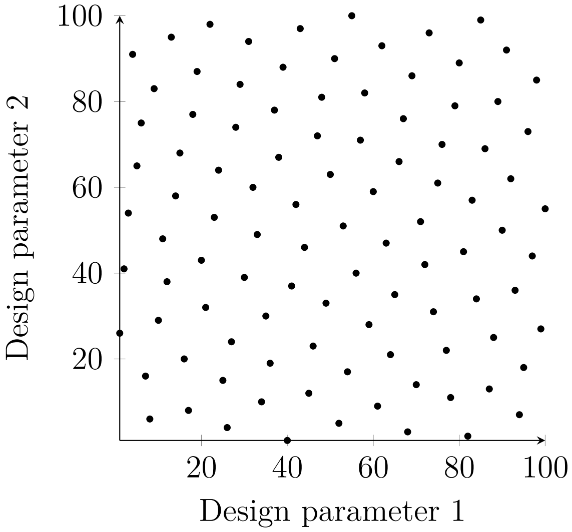

Figure 3.15: *Latin Hypercube sampling plan containing 100 points.*

The weights w_i are solved for exactly by solving the linear system

$$\mathbf{Aw} = \mathbf{u} \tag{3.3}$$

where $\mathbf{A} = A_{ij} = \xi_i(\|x_i - x_j\|_2)$ and $\mathbf{u} = \mathbf{u}(\mathbf{x_i})$ are the objective function values for each sample. An additional regression term, λ, is added to the diagonal of $\mathbf{A}$, Equation (3.3). This relaxes the requirements of the surrogate model being strictly interpolating, reducing high-frequency oscillations when the objective function contains noise. Radial Basis Functions can exhibit poor performance if the scale between the input to output differs greatly between dimensions. To solve this, each design parameter is normalised and scaled with a linear scaling factor c_j.

The RBFs, ξ_i, used in the surrogate model are the gaussian, $\xi(r) = e^{-(\varepsilon r)^2}$, inverse quadratic, $\xi(r) = \frac{1}{1+(\varepsilon r)^2}$ and inverse multiquadratic, $\xi(r) = \frac{1}{\sqrt{1+(\varepsilon r)^2}}$ where ε is the width factor of each RBF.

The ridge regression term, λ, widths, ε, Radial Basis Function ξ_i and axis scaling c_j are treated as hyperparameters and are optimised using a leave-one-out objective function to improve the prediction performance. The equivalent structure of the surrogate model is shown in Figure 3.16.

Training of the surrogate model is stochastic, meaning different models are obtained each time the model is trained. This property is used to improve the surrogate model by repeatedly training several models on the same data. The median of the models is used as the estimate of the function and the standard deviation between the models is used as an estimate of the local surrogate model uncertainty. The optimisation process then picks designs that both explore the design space and exploits the current knowledge of the surrogate model. The model is then retrained as more designs are tested.

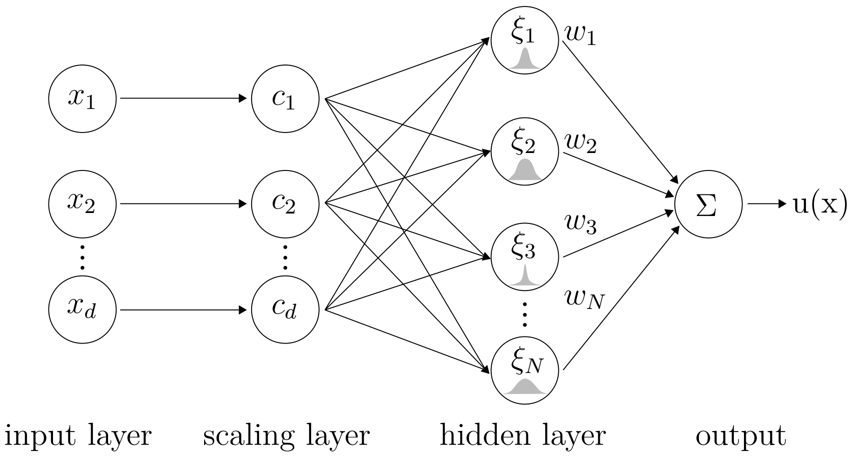

Figure 3.16: *Radial Basis Function surrogate model network structure.*

The surrogate model performance was good when compared to Random Sample, Differential Evolution, Nelder–Mead and Bayesian Optimisation; performing as well, or better than the other algorithms, on 17 out of 18 optimisation benchmark problems.

Chapter 4

Cavities

This chapter focuses on the wake behaviour at yaw using a straight cavity and a cycle averaged drag optimised tapered cavity, covering the main findings in Paper IV. The geometry used in this chapter is the Windsor model, presented in section 3.1.1. The cavity is compared to the vehicle without a cavity as well as a variant where the tapered cavity is filled to assess the influence of the tapering alone.

The numerical optimisation results are presented and discussed first followed by the wind tunnel results at 0°-yaw. Lastly, the results at yaw are shown. All the presented flow field and pressure results in this section are from the wind tunnel tests.

4.1 Cycle averaged drag optimised cavity

The cavity taper angles are optimised using the steady-state simulation approach to strike a balance between the cost of evaluating a design and the number of affordable iterations. The objective is to improve the cycle averaged drag performance, Equation (2.3). The sides are constrained in the optimisation to have the same angle while the roof and diffuser are separate design parameters thus resulting in three design parameters with a maximum tapering of 25°. Each objective function requires the simulation to be run at three yaw angles, which are re-meshed between each run since the tunnel geometry is also simulated. A total of 42 objective functions, or 126 simulations, is run in the optimisation of the cavity tapering. The optimisation was stopped once it was deemed that no further significant improvement could be found in the vicinity of the already tested designs. The best found design features a roof angle of 12.6°, diffuser angle of 1° and side tapering of 13.5°. Many designs had similarly low drag at 0°-yaw with as much as 5 % more cycle averaged drag compared to the best design. This highlights the usefulness of the cycle averaged drag value for optimisation. The optimisation convergence is shown in Figure 4.1. As shown in the method section, the steady-state simulation approach is less accurate than the unsteady approach on such an inherently unsteady geometry. An open question that remains, is the influence of the computational accuracy on the final optimisation result.

The sensitivity to the design parameters was tested using the surrogate model to predict the cycle-averaged drag in the entire design space. Figure 4.2 shows the design sensitivity for the roof and side taper angle for the lowest diffuser angle.

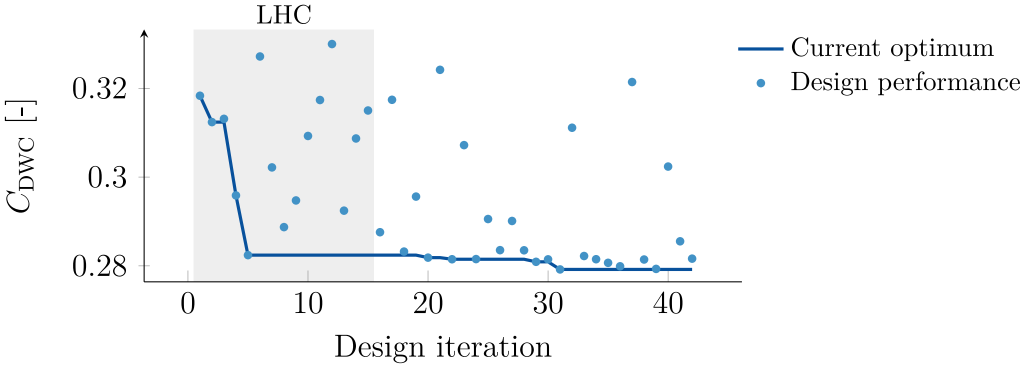

Figure 4.1: *Cavity optimisation history.*

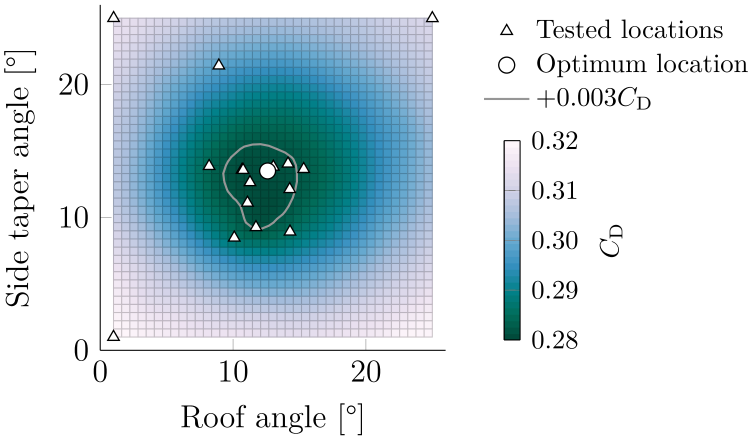

Figure 4.2: *Sensitivity to roof- and side taper-angle for a fixed diffuser angle of* 1°*. Tested design locations include all designs with a diffuser angle below* 2°*.*

The design area within 10° to 15° in both side tapering and roof tapering angle is within approximately 0.003 C_{D} of the optimum location. All the simulated designs with a diffuser angle within 1° of the optimum are shown to highlight the sample coverage in the vicinity of the optimum. The sensitivity to changes is low near the optimum according to the predictions from the RANS simulations.

Based on these results, a design with 14° side- and roof-tapering with a 0° diffuser was manufactured. The side and roof tapering was selected at angles larger than the optimum to allow easier addition of surfaces to the outside of the cavity. The final manufactured design is shown in Figure 4.3. The following results in this chapter are from the wind tunnel experiments in the Loughborough University Large Wind Tunnel unless explicitly compared to the numerical simulations.

4.1.1 0°-yaw

The force coefficients for the four configurations namely, square-back, straight cavity, tapered cavity, and the filled tapered cavity are given in Table 4.1. The

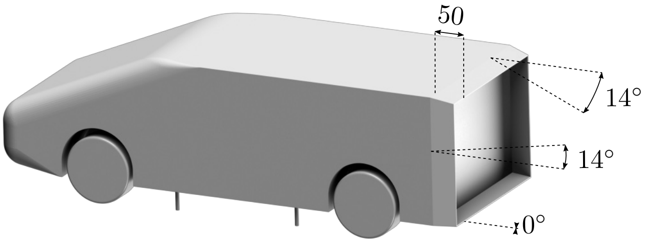

Figure 4.3: *Windsor geometry with wheels. Measurements are given in* mm.

Configuration.	C_{D}	C_{FL}	C_{RL}	C_{DB}
Square-back	0.389	0.142	0.002	0.291
Straight cavity	0.360	0.140	-0.007	0.259
Tapered cavity	0.320	0.121	0.166	0.200
Filled tap. cav.	0.335	0.124	0.166	-

Table 4.1: *Aerodynamic force coefficients at* 0°*-yaw.*

straight cavity reduced drag by $7.5 \pm 0.4\,\%$ compared to the square-back. In total, a $17.6 \pm 0.4\,\%$ reduction in drag is achieved with the tapered cavity compared to the square-back. The cavity on the tapered geometry reduces drag by, $4.5 \pm 0.4\,\%$, compared to the filled taper. The drag reductions from the cavity and taper are not directly additive. However, there is still a significant reduction in drag when both a cavity and taper is combined. It is worth noting that the square-back is shorter than the other geometries which can exaggerate the drag difference.

The base pressures are shown in Figure 4.4 where the square-back and straight cavity have high-pressure zones towards the top of the geometry while for the tapered cavity it is located towards the bottom. The base pressure is higher for the tapered cavity, evident by the reduction in base drag, C_{DB}, Table 4.1, while the base pressure is more uniform compared to the other configurations.

Figure 4.5 shows the centerline velocity for each configuration. The square-back and straight cavity are upwash dominated. The tapered cavity is downwash dominated, consistent with the base pressure, Figure 4.4. This is an unexpected result as typically low drag geometry is associated with the return flow direction in the wake being aligned with the freestream [42, 43]. This is referred to as a balanced wake, i.e. the wake is neither upwash nor downwash biased.

The filled tapered cavity wake is shorter and slightly taller compared to the tapered cavity. This reduction in length is associated with higher levels of unsteadiness and mixing in the shear layers. This results in increased entrainment of the freestream flow in the wake which increases drag [16]. This is confirmed by analysing the turbulent kinetic energy in the shear layer with larger fluctuations for the filled tapered cavity, Figure 4.6.

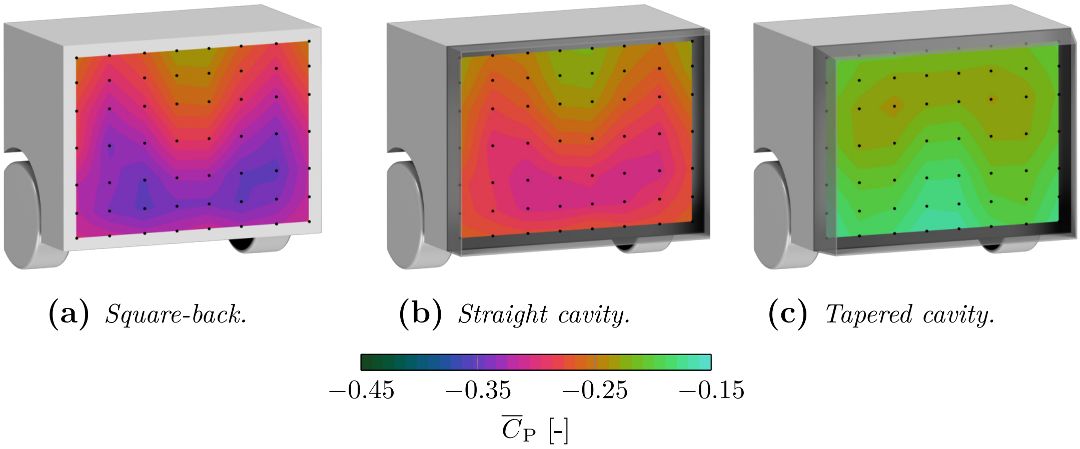
(a) *Square-back.* (b) *Straight cavity.* (c) *Tapered cavity.*

Figure 4.4: *Base pressure at 0°-yaw. The pressure tap locations are marked in black.*

The base pressure fluctuations are reduced by the addition of a cavity and further reduced with the taper, Figure 4.7, with areas of largest fluctuation located near the impingement location.

Figure 4.8 shows the base coefficient of moment around the horizontal and vertical midpoint. The widths of the lateral and vertical PDFs decrease with decreases in drag indicating that the strength of the large scale movement of the wake is reduced by the cavity and further reduces with the tapering.

The wake is commonly characterised by coherent motions called flapping and pumping. Flapping is related to the vertical or horizontal side to side movement of the wake. Duell et al. [17] described the pumping motion as a vortex pair leaving the wake causing the bubble pumping of the wake when the vortices shed. Pumping is expected to act in the stream-wise direction primarily. Figure 4.9 shows the Power Spectral Density of the centre of pressure (CoP) movement on the base. The high-frequency peaks at $St = 0.7$ are related to the wind tunnel fan [44]. The pumping motion has been related to the low-frequency peaks, $St = 0.08 - 0.1$, and the flapping to the high-frequency peaks, $St = 0.19$ and $St = 0.23$ [17, 18]. All geometries exhibit peaks in the flapping frequencies, however, peaks in the range of pumping motion are only seen in the geometries with cavities. This also indicates that the pumping motion is coupled to the vertical and lateral motion of the wake as pure longitudinal motion is not captured by the base pressures. Analysis of the individual pressure taps revealed the same trends as the centre of pressure movement.

The PDF of the centre of pressure movement was also investigated, Figure 4.10. The CoP movement is related to the balance in the wake and is different from the base moment coefficient, Figure 4.8, which shows the strength of the fluctuations. The distribution in the vertical direction is similar between the geometries, however, the lateral CoP movement is reduced by the tapering. The smaller differences

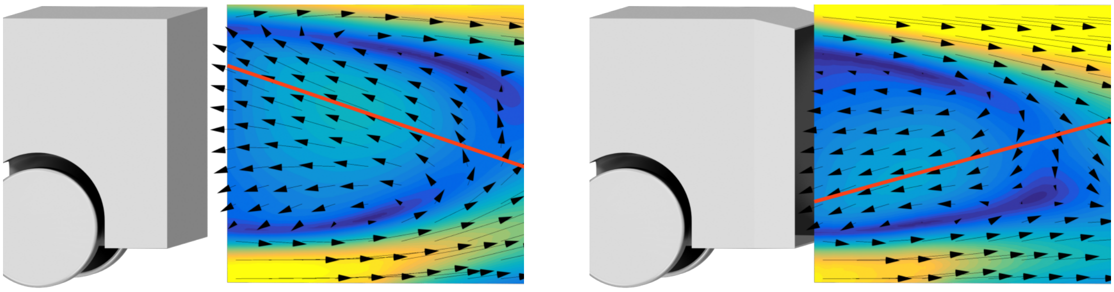

(a) *Square-back.* **(b)** *Tapered cavity.*

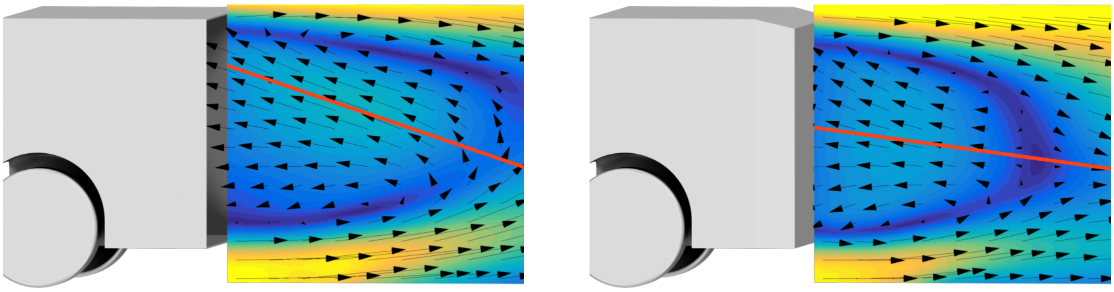

(c) *Straight cavity.* **(d)** *Tapered filled cavity.*

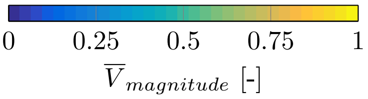

Figure 4.5: *Normalised centreline velocity magnitude at 0°-yaw. The red line is added to indicate the wake balance and is positioned manually where the velocity towards the base is large.*

in CoP movement with the simultaneously larger difference in base moment coefficient suggest that the wake is able to move using less force for the lower drag configurations. This can be thought of as a seesaw effect where a lighter seesaw, or reduction in base drag, requires less force for the same movement.

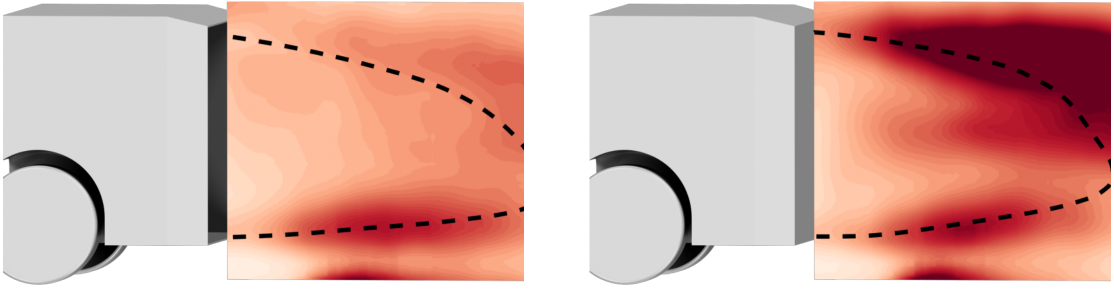

(a) *Tapered cavity.* **(b)** *Tapered filled cavity.*

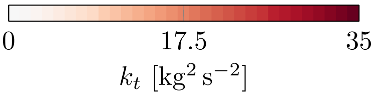

Figure 4.6: *Time-averaged turbulent kinetic energy at the centreline. The line represents the wake where the longitudinal velocity is 25 % of V_∞.*

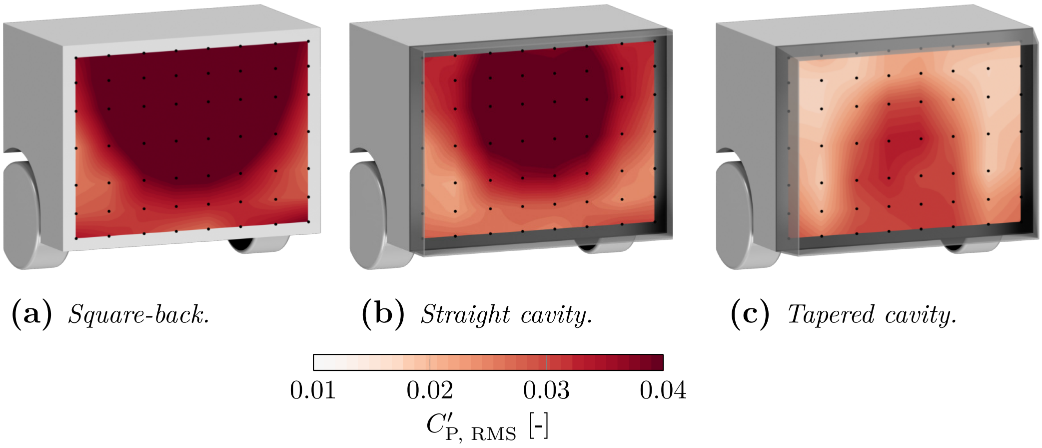

(a) *Square-back.* **(b)** *Straight cavity.* **(c)** *Tapered cavity.*

Figure 4.7: *Base pressure fluctuations at* 0°*-yaw. The pressure tap locations are marked in black.*

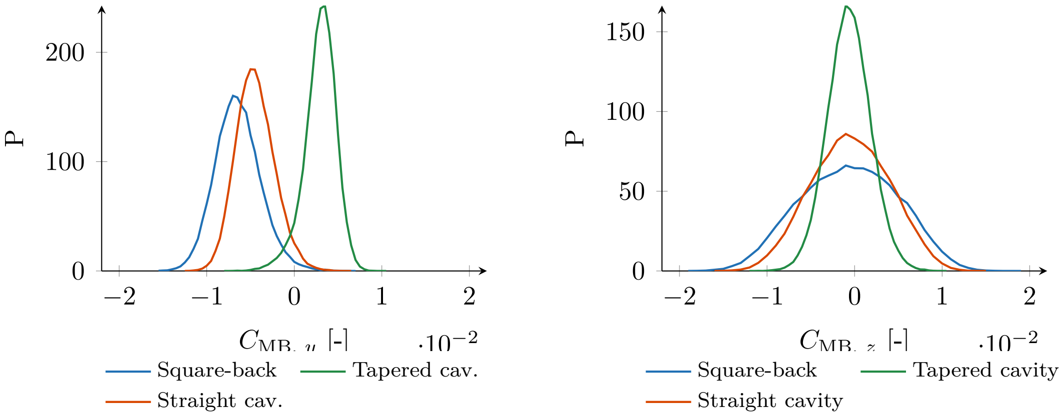

(a) *Coefficient of base moment around the horizontal axis at the base midpoint.*

(b) *Coefficient of base moment around the vertical axis at the base midpoint.*

Figure 4.8: *Probability Density Function (PDF) of the base moment coefficient at* 0°*-yaw.*

Varney [33] investigated the effect of cavity depth on the Windsor geometry without wheels, which is laterally bi-stable. A laterally bi-stable wake randomly switches between two lateral symmetry breaking modes. As the cavity depth was increased, the pumping motion was reduced and the wake was no longer bi-stable. This was attributed to a dampening effect due to the increased wake volume. Bonnavion et al. [22] investigated vertical symmetry breaking modes that produce an upwash or downwash dominated wake depending on the vehicle pitch. Altering the pitch slightly could force the downwash or upwash state. However, for some pitch angles, the wake switched randomly between the upwash or downwash dominated states, similar to a laterally bi-stable wake [18, 45]. The lowest drag was found at the transition where random switching between the states occurs which has been found by several authors [18, 22, 46]. Evrard et al. [20] explained the reduction in drag for the bi-stable geometries as the switching event being lower drag than either of the asymmetric states, making it beneficial for a geometry to

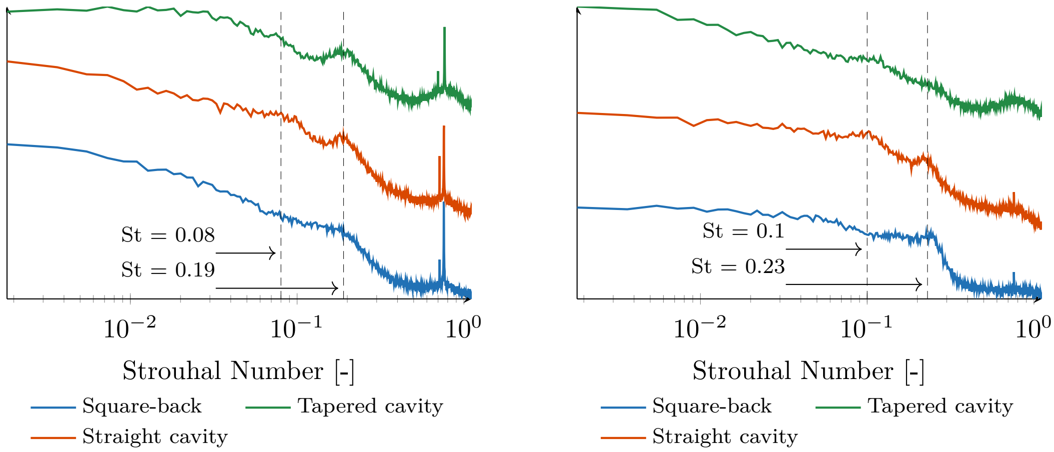

(a) *Lateral movement.* **(b)** *Vertical movement.*

Figure 4.9: *Power Spectral Density (PSD) of centre of pressure movement at 0°-yaw. The Strouhal number is normalised by the square root of the vehicle frontal area and freestream velocity.*

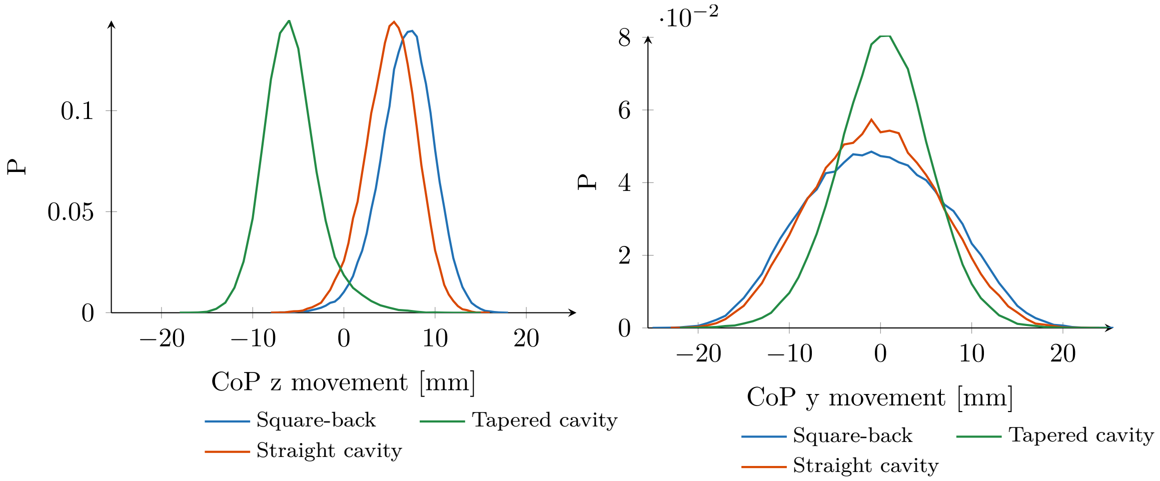

(a) *Centre of pressure movement in the vertical direction.*

(b) *Centre of pressure movement in the horizontal direction.*

Figure 4.10: *Probability Density Function (PDF) of the base centre of pressure at 0°-yaw. The midpoint of the base is defined as 0.*

be switching between the states rather than being forced into one state. Pavia et al. [18] findings suggest that a certain degree of pumping in the wake is needed to switch between bi-stable states.

All geometries were investigated for switching symmetry breaking modes in the lateral and vertical direction for each yaw angle. Similar geometries have shown bi-stable behaviour where the wake randomly switches between vertical or lateral symmetry breaking modes [45, 47–49]. No evidence of symmetry breaking modes was found here which is consistent with the Windsor model with wheels [33]. The wheels are known to introduce additional upwash, locking the wake into a vertically

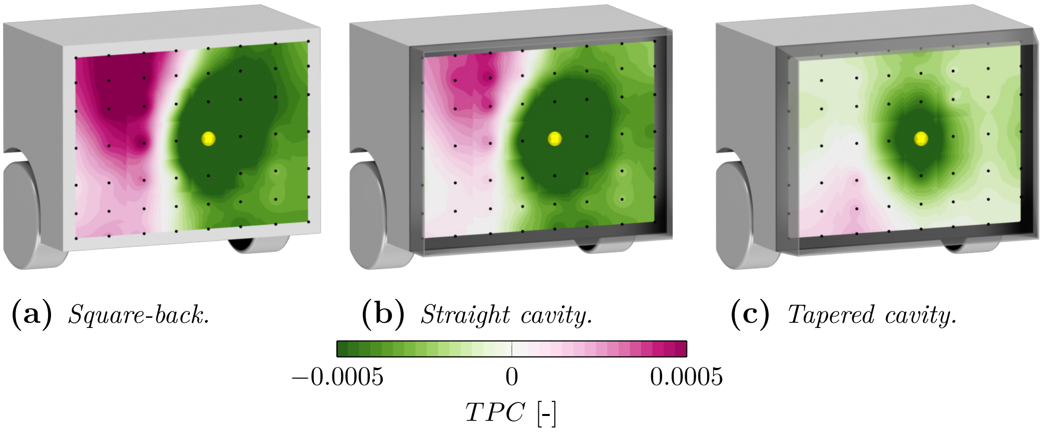

(a) *Square-back.* **(b)** *Straight cavity.* **(c)** *Tapered cavity.*

Figure 4.11: *Two-point correlation at the pressure tap marked with a yellow sphere at* 0°*-yaw.*

asymmetric state [26].

The two-point correlation was investigated for each pressure tap on the base, Figure 4.11 shows the results for a centrally located tap. The straight and tapered cavity are mainly positively correlated, consistent with the pumping motion, while the square-back is dominated by the lateral flapping. The points located at the sides (not shown here) indicate a strong flapping motion for the square-back and straight cavity while being weaker for the tapered cavity. This is consistent with the narrower distribution of centre of pressure movement for the tapered cavity, Figure 4.10b. No evidence of vertical flapping was found in the TPC, however, this does not exclude the presence of vertical flapping.

As Varney [33] also noted, there is no clear consensus between the observed wake motions and drag. Removing the large unsteady movements in the wake can reduce drag. However, balancing the wake, introducing the large scale unsteady movements, reduces drag. In the present work, adding the straight cavity to the square-back geometry introduces the low-frequency mode associated with pumping.

The Windsor model with wheels introduces additional upwash compared to the model without wheels. The absence of the pumping frequencies for the square-back geometry in this work is thought to be due to the wake being locked into a more stable, upwash dominated state. This stable, but high drag, state hinders the pumping motion of the wake. The results indicate that as the wake becomes more balanced, it is able to move more freely, introducing large scale wake motion. The introduction of large scale wake motion from balancing the wake relates to a reduction in drag in this work. For further drag reduction, it can be beneficial to dampen out the large scale wake motions, for example by increasing the cavity depth [20, 33], introducing a control cylinder [20, 50], actively symmetrising the wake with jets [51] or adding a splitter plate [52]. This forces the wake to spend more time in the symmetric, low drag, state.

The results indicate that the additional drag reduction from the tapering is

Configuration	C_{D}	C_{FL}	C_{RL}	C_{DB}	C_{Yaw}
5°-yaw					
Square-back	0.435	0.171	0.008	0.322	-0.082
Straight cavity	0.425	0.174	-0.003	0.308	-0.081
Tapered cavity	0.354	0.151	0.183	0.226	-0.124
Filled tap. cav.	0.367	0.159	0.170	-	-0.119
10°-yaw					
Square-back	0.482	0.252	0.032	0.357	-0.160
Straight cavity	0.476	0.259	0.024	0.350	-0.157
Tapered cavity	0.378	0.269	0.242	0.256	-0.209
Filled tap. cav.	0.389	0.277	0.227	-	-0.202

Table 4.2: *Aerodynamic force coefficients at yaw.*

primarily due to the improved balance and reduced wake size. However, the reduction in unsteadiness, allowing the wake to spend more time in a symmetric state, is also beneficial.

4.1.2 5° & 10°-yaw

The aerodynamic coefficients for each configuration at yaw is presented in Table 5.2. All the flow field and pressure data presented in this section is at 5°-yaw. The geometries retain their relative ranking at yaw with reductions from using a cavity and further reductions in drag with the taper.

At 5°-yaw the wake becomes upwash dominated at the centreline for all the investigated configurations. Figure 4.12 shows the tapered cavity wake at 5°-yaw which at 0°-yaw had a downwash dominated wake, Figure 4.5b. The base pressure distributions are consistent with centreline observations, indicating a predominately upwash dominated wake with a high-pressure zone in the top windward corner, Figure 4.13. The tapered cavity has a more uniform base pressure distribution compared to the other configurations.

The wake is highly 3-dimensional, especially at yaw as it is no longer laterally symmetric when time-averaged. Figure 4.14 shows the crossflow in the near wake behind the vehicle. The crossflow is defined as the magnitude of the lateral and vertical velocity components. The crossflow in the near wake is lower for the straight cavity compared to the square-back and it is the lowest for the tapered cavity. Filling in the tapered cavity also increases the near wake crossflow velocities. The optimisation objective for the tapered cavity was the cycle-averaged drag, the unexpected downwash at zero yaw is a result of the trade-off in performance between each yaw angle as the geometry becomes increasingly upwash dominated

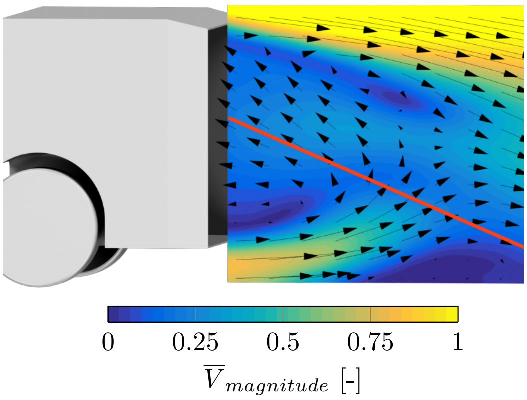

Figure 4.12: *Normalised centreline velocity magnitude for the tapered cavity at 5°-yaw. The red line is added to indicate the wake balance and is positioned manually where the velocity towards the base is large.*

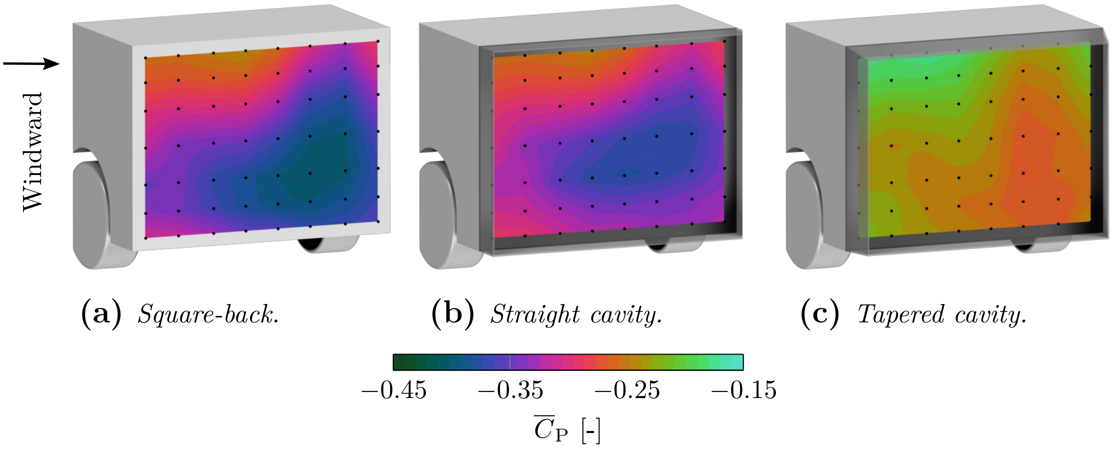

(a) *Square-back.* **(b)** *Straight cavity.* **(c)** *Tapered cavity.*

Figure 4.13: *Base pressure at 5°-yaw. The pressure tap locations are marked in black.*

at yaw.

Crossflow in the near wake is used in this thesis as an indicator of wake balance. A balanced wake, where the flow in the wake impinges the base with low lateral and vertical velocity components has been linked to decreases in drag [33, 53].

Figure 4.15 shows the base pressure fluctuations at 5°-yaw. The fluctuations are generally reduced compared to the 0°-yaw. The PDFs of the base moment coefficients and CoP were also investigated at 5°-yaw. The distributions are more similar between each configuration. The results indicate that the upwash in the wake caused by yawing the model is driving the wake behaviour. This is also evident in the base pressure distribution where the distribution is qualitatively similar, Figure 4.13.

The PSD of the centre of pressure at yaw, Figure 4.16, does not show any

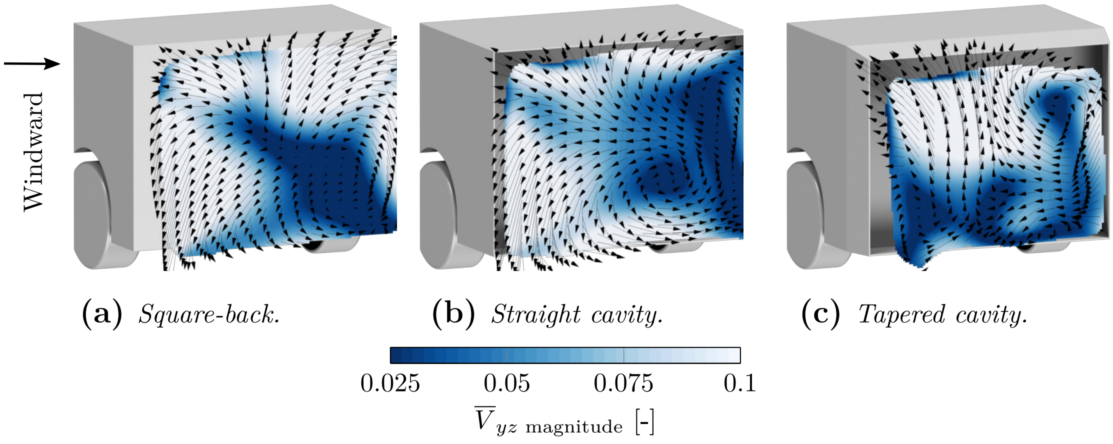

(a) *Square-back.* (b) *Straight cavity.* (c) *Tapered cavity.*

Figure 4.14: *Crossflow velocity magnitude* 75 mm *behind the base at* 5°*-yaw. The values are normalised by* V_∞ *and clipped where the longitudinal velocity is larger than* 25 % *of* V_∞*.*

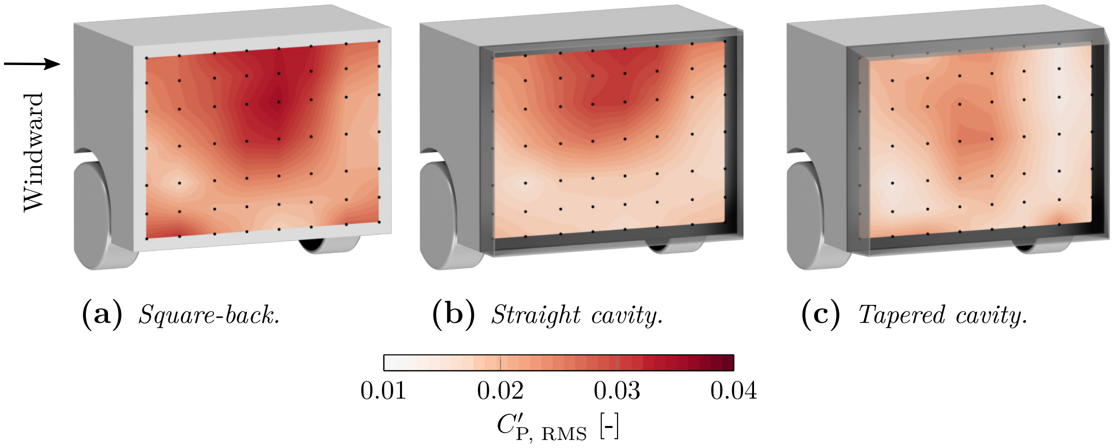

(a) *Square-back.* (b) *Straight cavity.* (c) *Tapered cavity.*

Figure 4.15: *Base pressure fluctuations at* 5°*-yaw. The pressure tap locations are marked in black.*

clear peaks consistent with the flapping motion in the vertical direction. This is consistent with the theory that the wake becomes more stable, hindering large scale movement, as the wake becomes upwash dominated at yaw. The lateral CoP movement indicates flapping, $St = 0.23$, for all configurations, however, it is only the tapered cavity that shows a clear peak in the pumping region, $St = 0.06$. This is thought to be due to the improved wake balance for the tapered cavity.

The shear layers were compared between the configurations with cavities and those without. Generally, the geometries with cavities have more concentrated shear layers with less fluctuation. Figure 4.17 shows the vorticity on the complete wake at 5°-yaw for the highest and lowest drag configurations. With a cavity, the flow in the cavity can re-align to the freestream flow direction before reaching the trailing edge, reducing the shear layer mixing. This is also evident at 0°-yaw. The

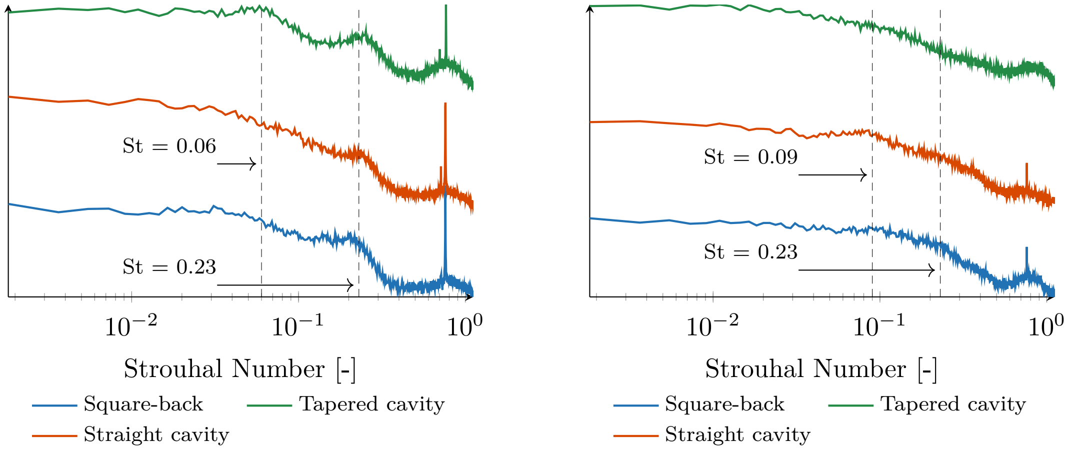

(a) *Lateral movement.* **(b)** *Vertical movement.*

Figure 4.16: *Power Spectral Density (PSD) of centre of pressure movement at* 5°*-yaw. The Strouhal number is normalised by the square root of the vehicle frontal area and freestream velocity.*

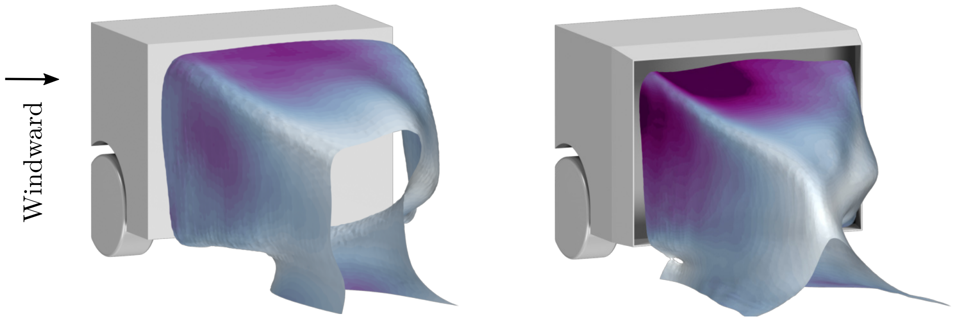

(a) *Square-back.* **(b)** *Tapered cavity.*

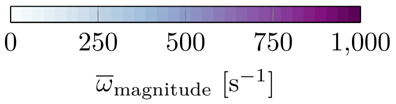

Figure 4.17: *ISO surface of* $\overline{V}_x$ *at* 7.5 m/s *for* 5°*-yaw coloured by the vorticity magnitude.*

internal walls of the cavity also provide resistance to crossflow in the wake as they provide solid boundaries where more of the kinetic energy can be converted to pressure. This explains part of the damping effect of cavities in conjunction with the added mass in the wake as discussed by Varney [33]. This is also consistent with the observations by Luckhurst et al. [53] where lower near-wall velocities improved drag.

Figure 4.18 shows the drag for each yaw angle as well as the driving cycle equivalent drag value, Equation (2.3). Cavities are effective at reducing drag, also at yaw. Varney [33] and Sterken et al. [27] showed that the drag at yaw benefits from increasing cavity depths. This suggests that further reductions in drag are

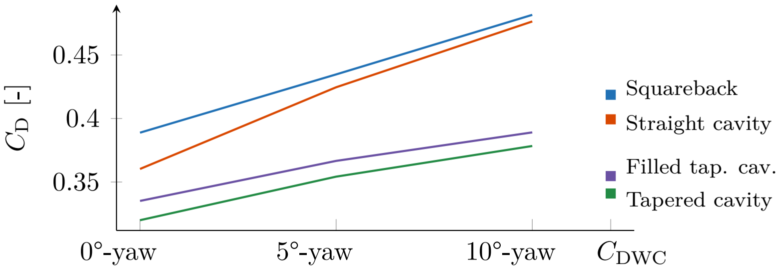

Figure 4.18: *Drag for each yaw angle and the driving cycle equivalent drag value.*

possible for a deeper cycle averaged drag optimised tapered cavity.

The optimisation of the cavity led to a geometry that is downwash dominated at 0°-yaw. Other designs had lower drag at 0°-yaw, but higher cycle averaged drag, during the optimisation of the cavity which featured a less tapered roof and more taper on the diffuser. This highlights the usefulness of considering a broader range of operating conditions when developing a vehicle. In total, an $18.6 \pm 0.3\,\%$ reduction in the cycle averaged drag is achieved by using the tapered cavity compared to the square-back. The straight cavity improves the cycle averaged drag by approximately $4.7 \pm 0.3\,\%$ compared to the square-back and $3.9 \pm 0.4\,\%$ for the tapered cavity compared to the filled tapered cavity geometry.

The RANS optimisation process predicted a 14.7 % improvement from the tapered cavity over the square-back. This is a smaller predicted improvement than what was found in the wind tunnel, however, even though the predictions differ it still highlights the potential benefits of using lower fidelity, lower cost, but fast simulations to optimise the vehicle geometry. There are also several documented improvements to this process that were not explored here such as combining the results from low fidelity and high fidelity simulations to create an affordable, but more accurate, surrogate model [54].

When optimising the cavity, each design was evaluated at each yaw angle to create a surrogate model of the cycle averaged drag. A more efficient approach can be to create a model for each yaw angle instead. The surrogate model is evaluated for each yaw angle separately and infill samples are added which gives the greatest improvements to the surrogate model's accuracy for each independent yaw angle. This is explored later in this thesis on the full-scale model with servo-controlled flaps.

Chapter 5

Cavities with trailing edge devices

This chapter covers the main findings in Papers I, III, and V.

5.1 Trailing edge kick

Sterken et al. [27] introduced the 3/4 tapered base cavity geometry used in this work. The smooth cavity gave the greatest reductions in drag at 0°-yaw. However, the variant with a kicked trailing edge flattened out the drag curve over the tested yaw angles, making the geometry more robust to side wind. The experimental base pressure distribution showed an increase in pressure in the top windward portion of the wake. This is further investigated here by analysing the complete wake using the unsteady numerical method.

The 0°-yaw results are presented and discussed first, followed by 5°-yaw. All results presented in this section are from the numerical simulations.

5.1.1 0°-yaw

Figure 5.1 shows the drag force relative to the square-back. Both cavities provide additional benefit for the tested yaw angles, however, the drag increase is smaller for the kicked cavity.

The position of the impingement location and the balance of the recirculating region has been reported as an important factor linked to drag [25]. In this work, the geometry with low drag has an impingement location which is moved downward resulting in a balanced wake, improving drag, Figure 5.2. A clear connection between any of the singular points and drag could not be found.

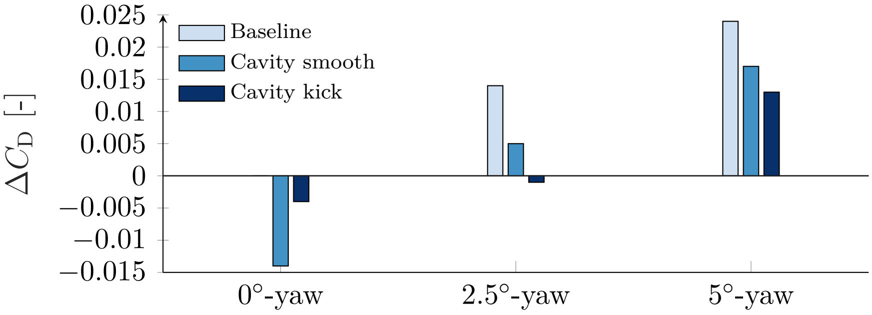

Figure 5.1: *Drag coefficient relative to the square-back.*

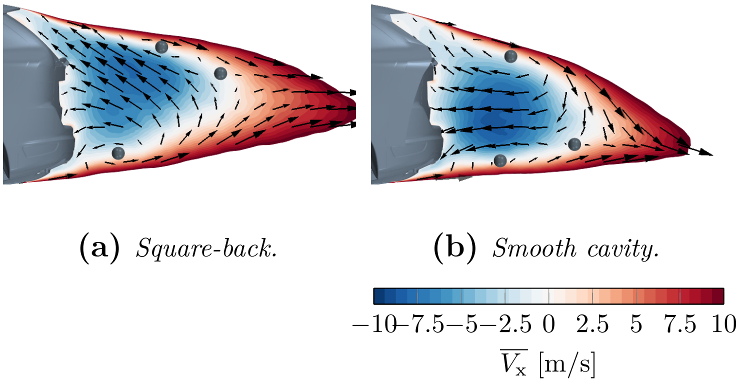

(a) *Square-back.* **(b)** *Smooth cavity.* **(c)** *Kicked cavity.*

Figure 5.2: *Mean longitudinal velocity with velocity vectors at 0°-yaw. Time-averaged singular points are marked with a sphere.*

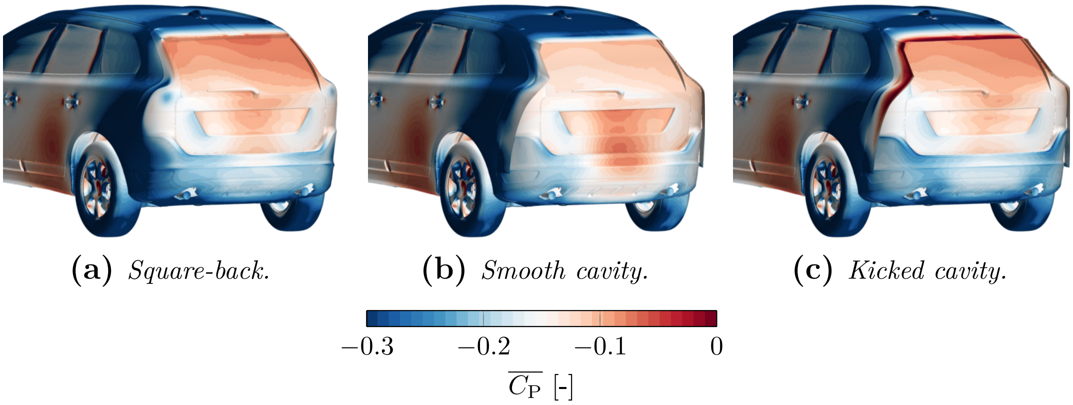

(a) *Square-back.* **(b)** *Smooth cavity.* **(c)** *Kicked cavity.*

Figure 5.3: *Mean surface pressure coefficient at 0°-yaw.*

The smooth cavity with a more balanced wake contains larger peak longitudinal velocities towards the base. The large longitudinal velocities with a direction perpendicular to the base are consistent with reduced drag. The improved base pressure recovery, as well as the moved impingement location, can be seen in Figure 5.3.

The two-point correlation of the unsteady base pressures was calculated for 33 locations distributed on the base. Figure 5.4 shows the two-point correlation for one of the positions to investigate lateral flapping. The strongest correlation is found for the smooth cavity which also has the most balanced wake. This is in line with the theory presented for the tapered cavity where a balanced wake produces more large scale coherent motion as it is freer to move. However, it is important to note that several aspects of the wake change simultaneously and the separation of different effects is not trivial.

The modal information for the three cases was also investigated using Proper Orthogonal Decomposition (POD). When POD is applied to a velocity field it extracts orthogonal modes by capturing the most amount of kinetic energy using the least amount of modes. More information on the POD method can be found in Paper I and also the works by Taira et al. [55] and Muld et al. [56]. Unsteady data was saved on the base and three planes in the wake of the vehicle, Figure 5.5.

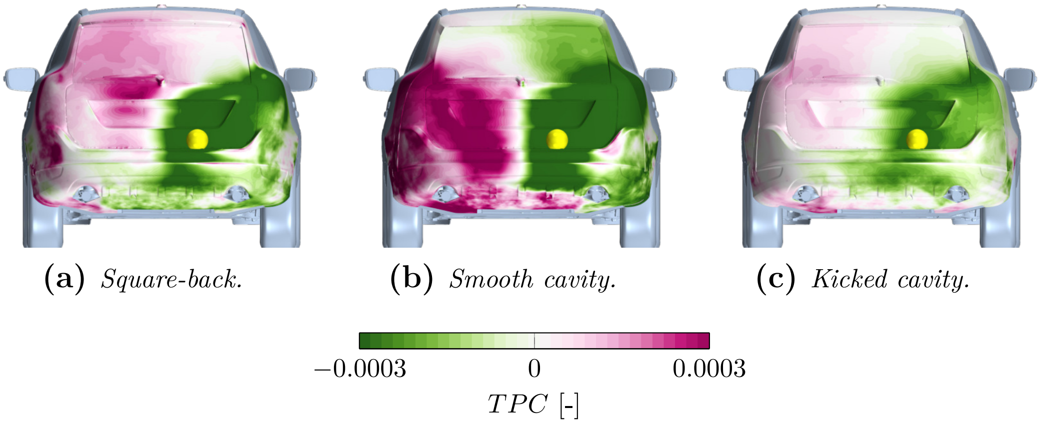

(a) *Square-back.* (b) *Smooth cavity.* (c) *Kicked cavity.*

Figure 5.4: *Two-point correlation at the point marked with a yellow sphere at* 0°*-yaw.*

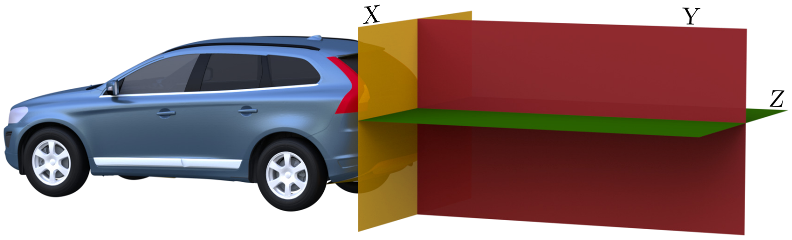

Figure 5.5: *Wake planes where time-resolved data is collected.*

Figure 5.6 shows the modal energy for each configuration at 0°-yaw. The first mode for the cavity with a kick is shown in, Figure 5.7. The first three modes are related to the shear layers for the square-back and kicked cavity. The lateral flapping motion is evident in the fourth mode for the square-back and the seventh mode for the kicked cavity. However, the first, the second and the fourth mode for the smooth cavity all indicate lateral flapping, the fourth mode can be seen in Figure 5.8. These results are not surprising considering the strong lateral two-point correlation for the smooth cavity.

The energetic fluctuations in the shear layer for the square-back and cavity with a kick are expected to increase entrainment of high momentum flow, shortening the wake and increasing drag [16]. The wake for the cavity with a kick is marginally

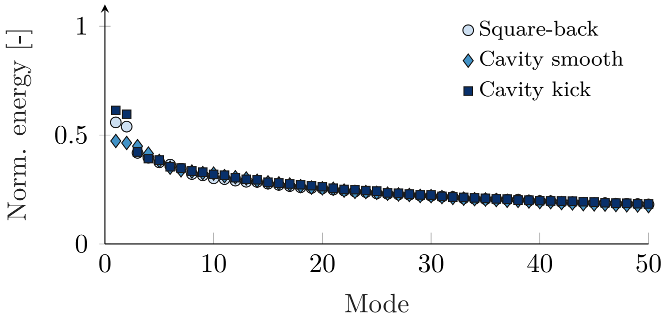

Figure 5.6: *Normalised energy of the 50 largest modes.*

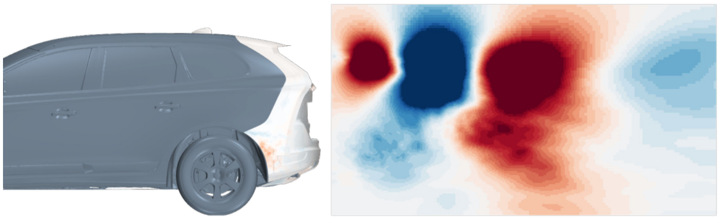

Figure 5.7: *Cavity with a kick at* 0°*-yaw. First POD mode, side view.*

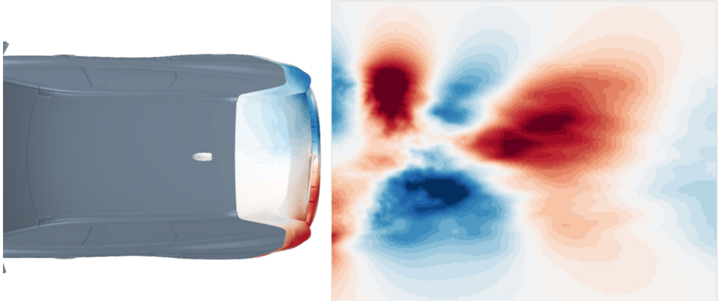

Figure 5.8: *Smooth cavity at* 0°*-yaw. Fourth POD mode, top view.*

shorter and also slightly lifted compared to the square-back. The improvement to drag for the cavity with a kick compared to the square-back is mainly due to the increase in pressure at the bumper near the rear wheels.

5.1.2 5°-yaw

The crossflow in the wake at yaw is shown in Figure 5.9. The square-back and smooth cavity are qualitatively similar with a large scale twisting motion in the wake. This large scale twisting structure is replaced by two smaller structures with the addition of the kick, illustrated schematically in Figure 5.10.

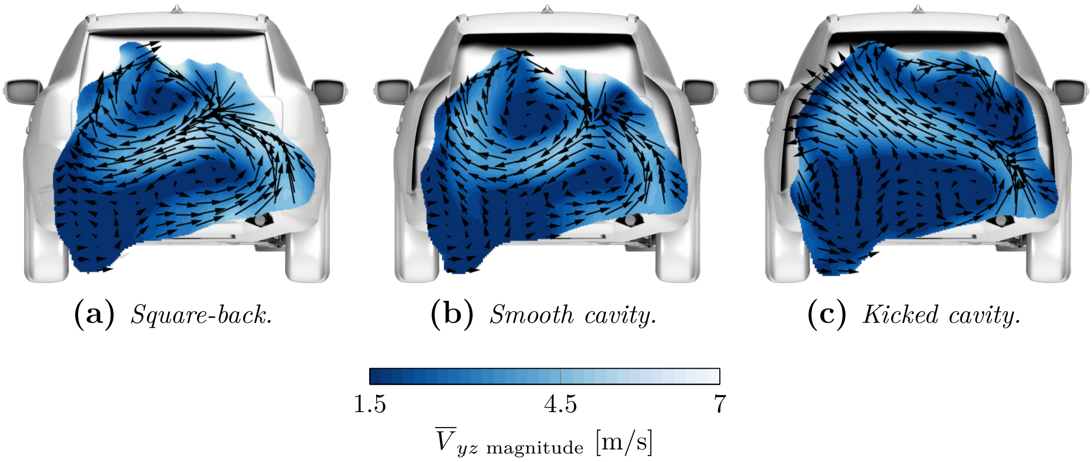

(a) *Square-back.* **(b)** *Smooth cavity.* **(c)** *Kicked cavity.*

Figure 5.9: *Mean crossflow with velocity vectors,* 300 mm *behind the vehicle at* 5°*-yaw.*

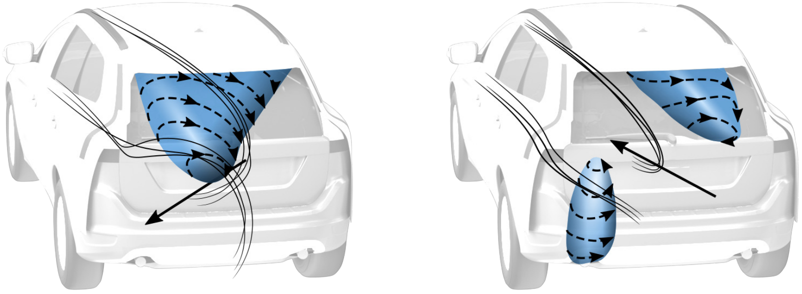

Figure 5.10: *Schematic overview of the wake twisting at 5°-yaw. Left smooth cavity, right cavity with a kick. The arrow on the base indicates the wake balance.*

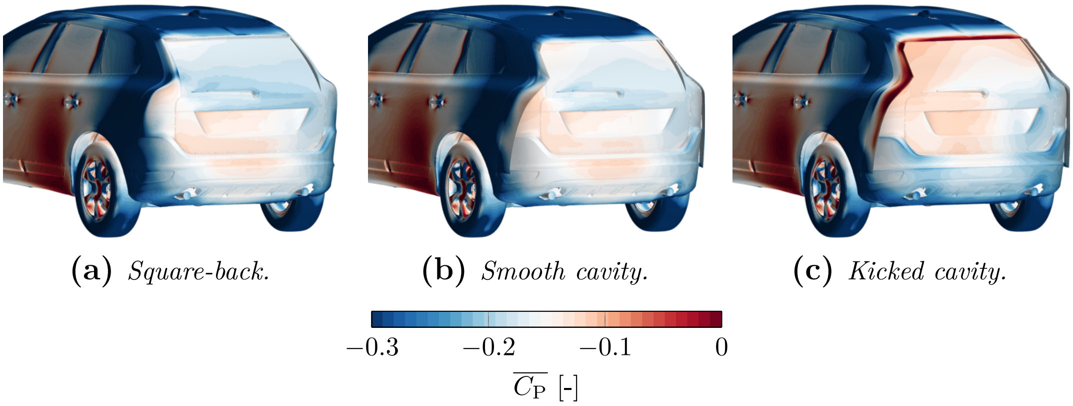

(a) *Square-back.* **(b)** *Smooth cavity.* **(c)** *Kicked cavity.*

Figure 5.11: *Mean surface pressure coefficient at 5°-yaw.*

The cavity with a kick reduces the crossflow in the wake, especially compared to the square-back. The lateral symmetry is also improved by the kicked cavity. The slight upwash of the kicked cavity can be seen in the base pressures, Figure 5.11, with the high-pressure area in the top windward corner. This upwash is thought to be preferred for the 3/4 cavity used here due to the internal walls of the cavity. The solid boundary of the internal cavity walls allows more of the kinetic energy in the flow to be converted into pressure compared to the downwash dominated geometries where the bottom of the cavity is open.

Howell [11] showed that the drag is either positively or negatively correlated with the lift change at yaw depending on the shape of the vehicle. His findings are consistent with vehicles producing either upwash or downwash dominated wakes at yaw. The XC60 produces a downwash dominated wake at yaw while the previously presented Windsor body produces an upwash dominated wake at yaw. This explains why the Windsor body benefits from additional downwash while the XC60 benefits from additional upwash to counteract the balance change when yawed.

The coverage area of the kick was also investigated with additional configurations by applying the kick to only the sides and only the roof. The drag for both configurations was within $\pm 0.002 C_D$ of the kick covering the entire 3/4 cavity. Even though the change in drag is small, the change in pressure distribution is significant

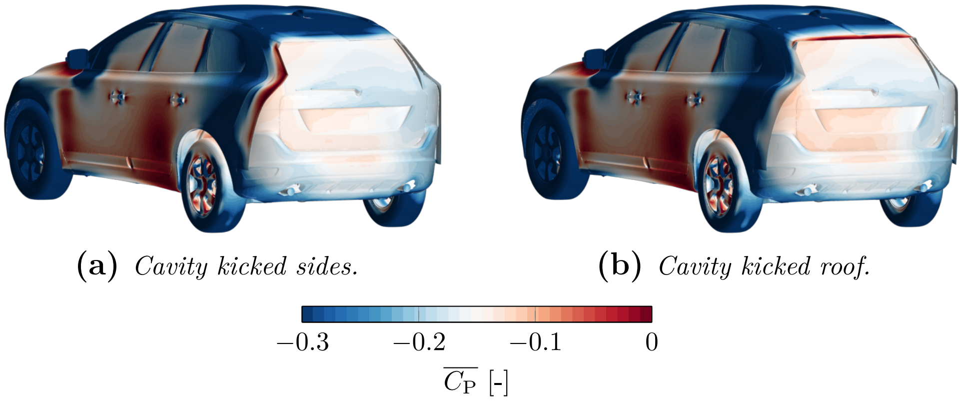

(a) *Cavity kicked sides.* **(b)** *Cavity kicked roof.*

Figure 5.12: *Mean surface pressure coefficient at* 5°*-yaw.*

between the three configurations, Figure 5.11c, 5.12a and 5.12b. This raises the question of which areas are more sensitive to yawed flow and whether other angles of the trailing edge kick would result in better performance.

5.2 Flaps on the Windsor body

The results from the kick coverage motivated the investigation presented in this section. The geometry is again Windsor body with the cycle averaged drag optimised cavity where nine additional trailing edge kicks, presented in Chapter 3, have been added, Figure 3.3. These kicked edges are now referred to as flaps since they can take on different angles at different sections of the cavity.

The angle of each flap is optimised for the different yaw angles. The previously presented surrogate model is used and the flap angle is changed manually in the wind tunnel for each configuration using one of the four fixed angles, 0°, 7°, 14° or 21°. All the presented results in this section are from the wind tunnel tests.

5.2.1 0°-yaw

A total of 26 unique designs were tested in the wind tunnel at 0°-yaw. The optimisation history of these tests can be seen in Figure 5.13. The optimisation process is split into two phases. The first phase optimises a design space that is constrained to two parameters, the roof and the sides where both sides have the same angle to maintain symmetry. The initial surrogate model is created from a Latin Hypercube containing 5 designs where one of the designs has all the angles set to 0°. This is the same as the cycle averaged drag optimised cavity discussed in Chapter 4, and will be referred to as the smooth design. Some results for the smooth cavity will be included again when comparing designs for convenience. The second phase allows all variables to be optimised independently, however, at 0°-yaw a symmetry constraint is used resulting in five design parameters instead of nine.

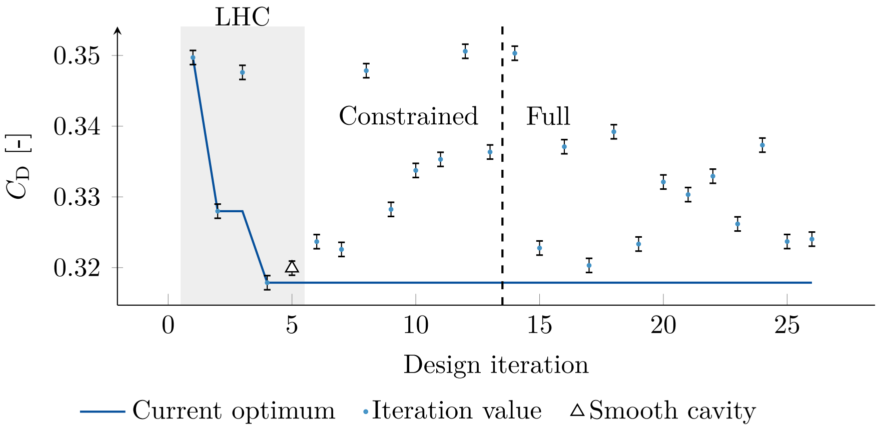

Figure 5.13: *Flap optimisation history at* 0°*-yaw. Error bars indicate the* 95 % *confidence interval.*

Configuration.	C_D	C_{FL}	C_{RL}	C_{DB}
Square-back	0.389	0.142	0.002	0.291
Smooth taper	0.320	0.121	0.166	0.200
Optimised flaps	0.318	0.125	0.121	0.201

Table 5.1: *Aerodynamic force coefficients at* 0°*-yaw.*

The force coefficients are given in Table 5.3 where the square-back and the smooth taper have been included again for convenience. An improvement of 0.002 C_D was found at 0°-yaw with 7° flap angles for all the roof positions and no flap angle on the sides.

The centreline velocity is shown in Figure 5.14 for the smooth taper and the optimised flaps. The flow for the optimised flaps results in a more balanced wake where the backflow is directed more perpendicular to the vehicle base. Buchheim et al. [57] showed that for longer roof tapering, larger reductions in drag were possible and the optimum taper angle increased with increasing length. This suggests that a longer taper in combination with longer flaps could improve drag even further.

The base pressure fluctuations are presented for the smooth taper and the optimised flaps in Figure 5.15. The overall fluctuations are increased by the increase in roof flap angle which is consistent with the previous observation that a more balanced wake exhibits more unsteadiness.

5.2.2 5° & 10°-yaw

Figure 5.16 contains the optimisation history of the 39 designs that were tested at 5°-yaw. At 10°-yaw 46 designs were tested with a similar optimisation history. Both feature the same optimisation procedure as for the 0°-yaw case, however, the geometry is no longer constrained to be symmetric.

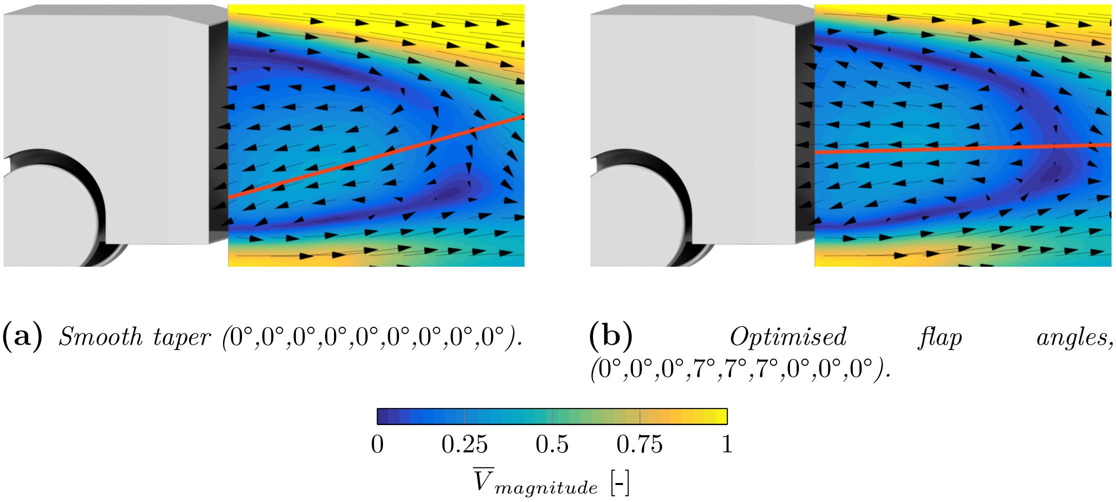

(a) *Smooth taper (0°,0°,0°,0°,0°,0°,0°,0°,0°).* **(b)** *Optimised flap angles, (0°,0°,0°,7°,7°,7°,0°,0°,0°).*

Figure 5.14: *Normalised centreline velocity magnitude at 0°-yaw. The red line is added to indicate the return flow direction and is positioned manually where the velocity towards the base is large.*

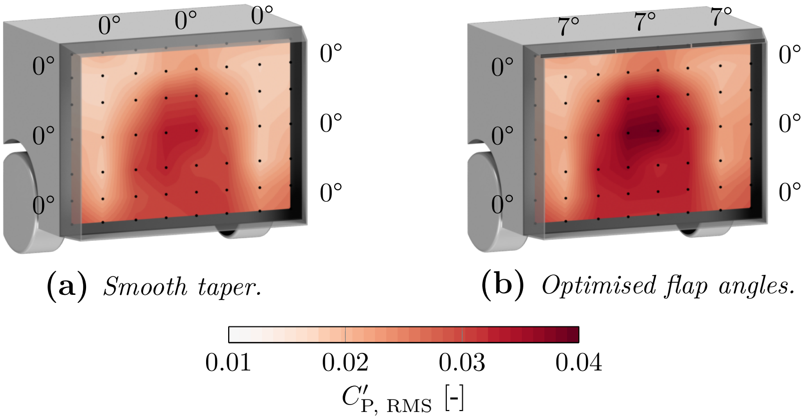

(a) *Smooth taper.* **(b)** *Optimised flap angles.*

Figure 5.15: *Base pressure fluctuations at 0°-yaw. The pressure tap locations are marked in black.*

No improvement in drag could be found in the constrained design space where the flaps on each side of the model have the same angle. This was unexpected as similar studies have shown that positive angles on the leeward side of the model have resulted in drag reductions [15, 58]. It was only possible to find an improvement (outside the reported confidence interval) over the smooth taper in the full design space.

The best performing design for both 5°- and 10°-yaw features the flap angles 0°,0°,0°,0°,0°,7°,0°,7°,14°, shown in Figure 5.17. Every design that had a significant drag reduction featured changes toward the leeward side of the model, flap positions (Figure 3.3) 6-9. Several designs have similar improvements to drag, but common to all designs with an improvement of 0.004 C_{D} or more is a non-zero flap on the roof's leeward side, position 6. This was an unexpected result, in fact, the configuration was re-tested to confirm the results. This finding is solely attributed

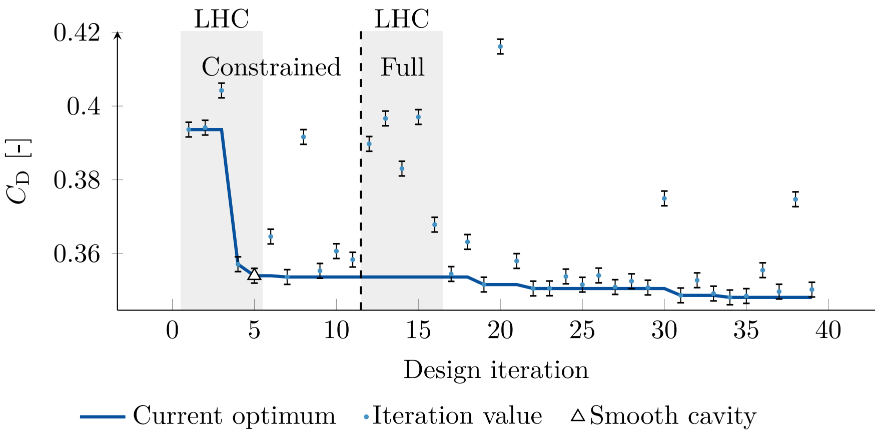

Figure 5.16: *Flap optimisation history at* 5°*-yaw. Error bars indicate the* 95 % *confidence interval.*

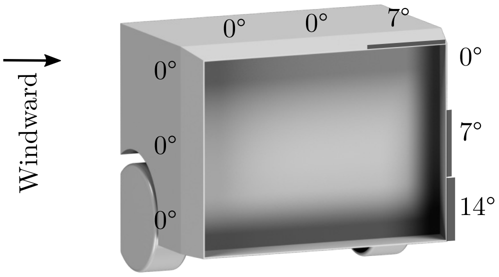

Figure 5.17: *Windsor geometry with optimised flap angles for* 5° *and* 10°*-yaw.* *(*0°,0°,0°,0°,0°,7°,0°,7°,14°*)*

to the use of an optimisation algorithm in this work and the reason for the positive flap in position 6 will be further explored in this section.

The force coefficients for the square-back, smooth taper and the optimised design are given in Table 5.2. A 0.006 C_D improvement was found for the optimised flaps over the smooth taper at 5°-yaw with a smaller improvement of 0.004 C_D at 10°-yaw. The driving cycle equivalent drag value for the square-back, smooth taper and optimised flaps are 0.419 ± 0.001, 0.341 ± 0.001 and 0.337 ± 0.001 C_DWC respectively. A 20 % reduction in the cycle averaged drag is achieved using the optimised flaps over the square-back. It would require additional energy to move the flaps actively and was not considered in this work.

Figure 5.18 shows the wake crossflow for the smooth taper, the optimised flap angles as well as the optimised flap angles with the leeward roof flap set to 0° to isolate the effects of flap number 6. The clockwise rotating structure in the top leeward corner has less downwash on the leeward side of the structure for the optimised flaps. The decrease in strength of this structure also reduces the crossflow at the bottom leeward portion of the wake. This is even true for the optimised configuration where the top leeward flap is set to 0°, Figure 5.18c.

The upwash on the windward side of the wake is reduced by the optimised flaps. This is observed in the base pressures where the top windward corner of the

Configuration	C_{D}	C_{FL}	C_{RL}	C_{DB}	C_{Yaw}
5°-yaw					
Square-back	0.435	0.171	0.008	0.322	-0.082
Smooth taper	0.354	0.151	0.183	0.226	-0.124
Optimised flaps	0.348	0.150	0.183	0.223	-0.133
10°-yaw					
Square-back	0.482	0.252	0.032	0.357	-0.160
Smooth taper	0.378	0.269	0.242	0.256	-0.209
Optimised flaps	0.374	0.270	0.240	0.254	-0.218

Table 5.2: *Aerodynamic force coefficients at yaw.*

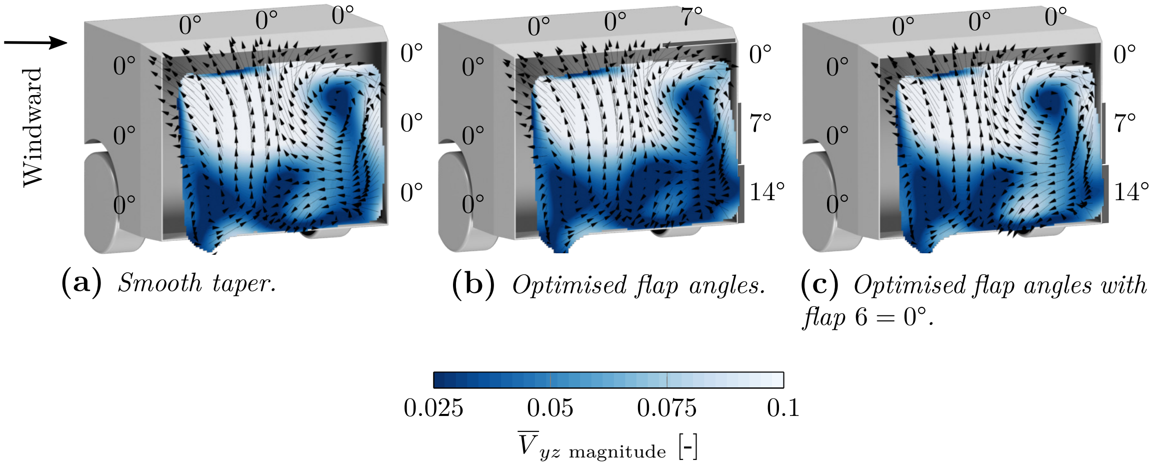

(a) *Smooth taper.* **(b)** *Optimised flap angles.* **(c)** *Optimised flap angles with flap* 6 = 0°.

Figure 5.18: *Crossflow* 75 mm *behind the vehicle base at* 5°*-yaw. The values are normalised by* V_∞ *and clipped where the longitudinal velocity is larger than* 25 % *of* V_∞.

optimised flaps has a slightly reduced high-pressure area, Figure 5.19b, compared to the smooth taper, Figure 5.19a. The base pressure is more symmetric for the optimised flap angles. This is consistent with observations in the literature for asymmetric base tapering in side wind [15].

One of the questions arising from the study of the trailing edge kick was which areas of the cavity are more sensitive in relation to drag. The drag sensitivity of each flap was investigated using the surrogate model of the tunnel results. The analysis changes the angle of only one flap at a time while keeping the other angles at the optimised design, in Figure 5.20. Some of the configurations were explicitly tested in the optimisation process and are indicated by a triangle, the others are estimated using the surrogate model. It is only designs that are explicitly run that are marked; however, several designs in close vicinity were also tested.

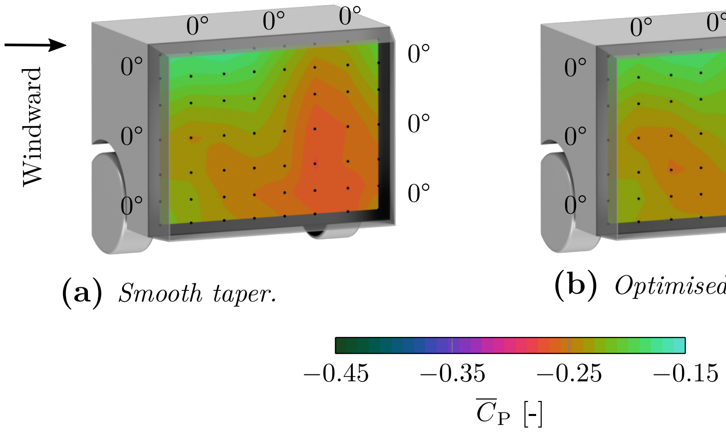

(a) *Smooth taper.* **(b)** *Optimised flap angles.*

Figure 5.19: *Base pressure at 5°-yaw. The pressure tap locations are marked in black.*

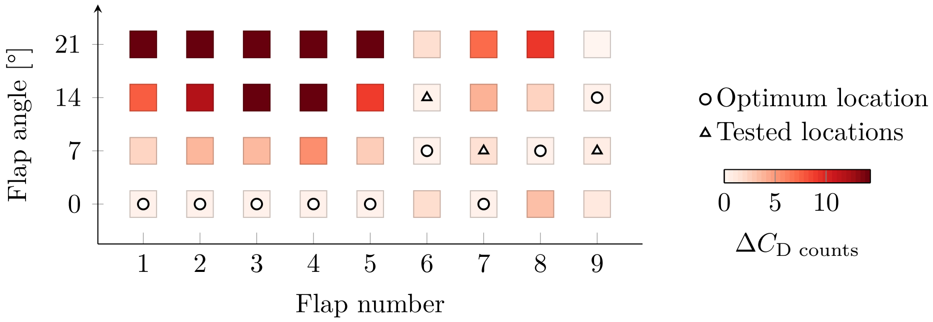

Figure 5.20: 5°*-yaw optimised design sensitivity to flap angle changes of each flap while keeping the other flap angles constant.*

The leeward flaps, positions 1 – 5, are the most sensitive to changes. The slope of the sensitivity for these flaps also suggests that negative angles could be beneficial. More tapering on the windward side has been shown to reduce drag at yaw, [15, 58], consistent with the results from the sensitivity analysis presented here. Based on the crossflow, Figure 5.18, the optimised flaps are generally directed against the vectors in the wake. This reduces crossflow and could be used as a qualitative tool when designing vehicles. Flap 7 carries a drag penalty for non-zero flap angles which is consistent with the optimised flap angles reducing crossflow in the wake.

Figure 5.21 shows the base pressure fluctuations of the smooth cavity and the optimised flaps at 5°-yaw which follow the same 0°-yaw trend where larger fluctuations are observed for the optimised configuration. This is also evident in the bulk wake flow where the turbulent kinetic is increased for the optimised flaps, Figure 5.22. However, the flaps are only positive in this work, contributing to an increased wake area at the separation point. When testing asymmetric tapering at yaw, Varney et al. [15] found that the asymmetric tapering angles that resulted in low drag also had high side force fluctuations, indicative of a balanced wake which is consistent with the findings here.

The addition of optimised flaps which are dependent on yaw angle further reduced

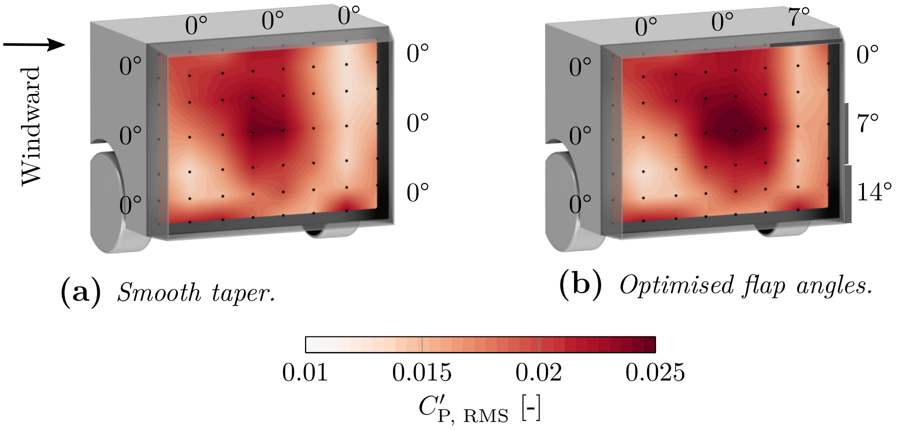

(a) *Smooth taper.* **(b)** *Optimised flap angles.*

Figure 5.21: *Base pressure fluctuations at* 5°*-yaw. The pressure tap locations are marked in black.*

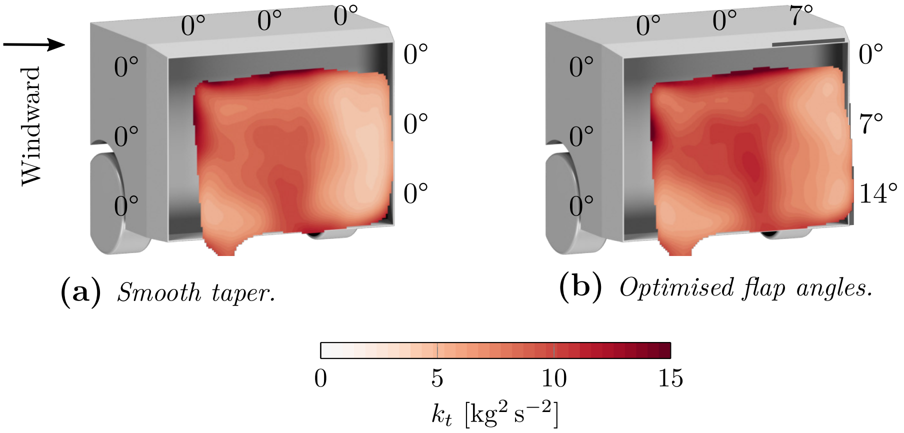

(a) *Smooth taper.* **(b)** *Optimised flap angles.*

Figure 5.22: *Time-averaged turbulent kinetic energy* 50 mm *behind the cavity at* 5°*-yaw. Clipped where the longitudinal velocity is larger than* 25 % *of* V_∞.

the cycle averaged drag by 2 % in this study compared to the already optimised cavity. The optimised wake flow featured less crossflow. At yaw, the flaps reduced the strength of a large scale rotating structure. A positive roof flap on the leeward side was featured in all designs with low drag.

The sensitivity analysis indicates that negative angles could further improve the yaw performance, especially on the windward side of the vehicle. The diffuser was kept constant in this study, however, it is reasonable to believe that it to can be used to improve the wake balance. If the flap system is implemented on a production vehicle, additional energy is needed as well as sensing of the flow direction which increases the complexity of such a system. Similarly to the cavity optimisation, the flaps could be optimised to reduce cycle averaged drag to produce a static design with good overall performance. These questions led to the investigation presented in the next section.

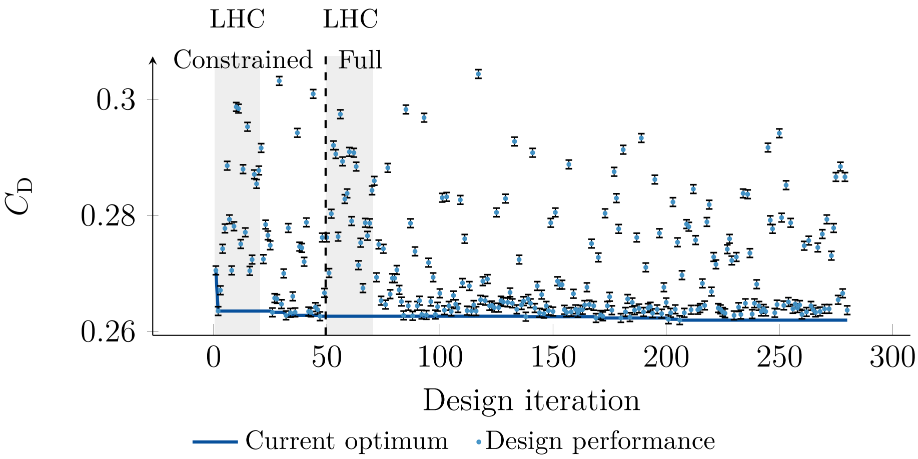

Figure 5.23: *Flap optimisation history at* 0°*-yaw. Error bars indicate the* 95 % *confidence interval.*

5.3 Flaps on the XC40

The previous results sparked the idea of extending the scope of trailing edge flaps on a base cavity to include negative angles and flaps on the floor. Optimising a static geometry for reduced cycle averaged drag using flaps is another aspect that is explored here. To do this efficiently on a physical object, servos were used to minimize the time spent between each configuration as the wind can be on continuously. All the presented results in this section are from the wind tunnel tests.

5.3.1 0°-yaw

The flaps were optimised for each angle separately using the same method as for the previous section. The cycle averaged drag optimisation was done by first optimising the geometry for each yaw angle separately while constraining it to symmetric designs and adding an additional 20 designs to explore the design space for the yawed cases. The cycle averaged drag was then optimised by running 5-10 designs at one yaw angle before switching yaw angle. This is a large benefit of surrogate model optimisation as the surrogate model information can be used and does not force a change of yaw angle for each new design as is required for some optimisation algorithms. In total 335, 245, 266 designs were tested at 0°-yaw, 5°-yaw and 10°-yaw respectively where 55 different cycle averaged designs were tested explicitly.

The optimisation history for 0°-yaw is shown in Figure 5.23 where 280 designs were tested. The largest improvements are found early in the optimisation routine with smaller improvements in the latter part.

Predictably, the geometry optimised for 0°-yaw has the lowest drag, Table 5.3. The smooth cavity, where all flaps are set to 0°, was also tested for comparison.

Configuration.	C_{D}	C_{FL}	C_{RL}	C_{DB}
Smooth cav.	0.280	0.027	0.137	0.088
0°-yaw opt.	0.263	0.023	0.081	0.069
Cycle ave. opt.	0.267	0.023	0.070	0.071

Table 5.3: *Aerodynamic force coefficients at* 0°*-yaw.*

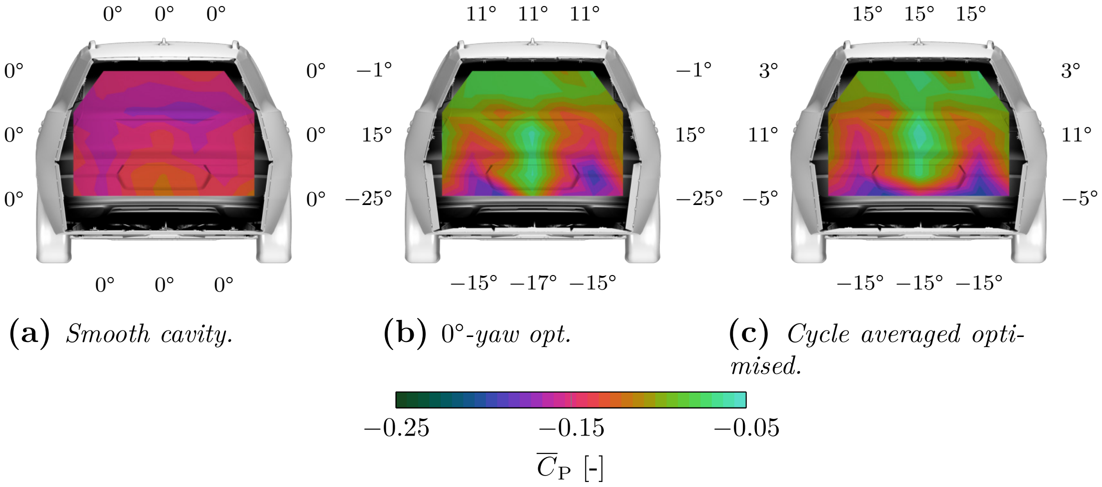

(a) *Smooth cavity.* **(b)** 0°*-yaw opt.* **(c)** *Cycle averaged optimised.*

Figure 5.24: *Base pressure at* 0°*-yaw.*

The base pressures, Figure 5.24, shows a distribution consistent with a balanced wake for the lower drag configurations. The smooth cavity has a pressure distribution consistent with downwash with a high-pressure region towards the lower part of the base. The high-pressure region for the cycle averaged drag optimised geometry is located further upward on the base compared to the 0°-yaw optimised geometry which is expected based on the roof angles.

The crossflow magnitude in the wake is shown in Figure 5.25. Measurements with a traversing unit are known to be intrusive, influencing the flow and vehicle drag [59]. However, the large scale trends in the wake are expected to be unaffected by the flow measurement technique. The lowest drag configuration has the least amount of crossflow with no clear bias towards upwash or downwash, consistent with the previously presented results in this thesis. The smooth cavity is downwash dominated while the cycle averaged optimised design is upwash biased. It is not obvious that the cycle averaged optimised geometry has significantly less drag than the smooth cavity. A centreline plane could better reveal the differences in upwash and downwash for the smooth cavity and cycle averaged drag optimised configurations, however, no centreline planes were measured. The slanted base may favour an upwash dominated wake, however, this requires further investigation.

The sensitivity to angle changes of each flap was analysed by changing the angle of one flap in ±2.5° and ±5° increments. The symmetric designs have a symmetry

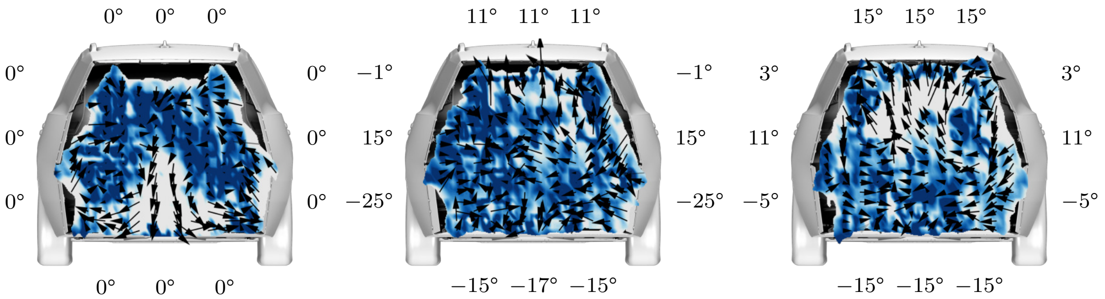

(a) *Smooth cavity.* **(b)** 0°*-yaw opt.* **(c)** *Cycle averaged optimised.*

Figure 5.25: *Crossflow velocity magnitude at 7 % of the vehicle length behind the vehicle at* 0°*-yaw. The values are normalised by* V_∞ *and clipped where the total pressure coefficient is larger than 0.*

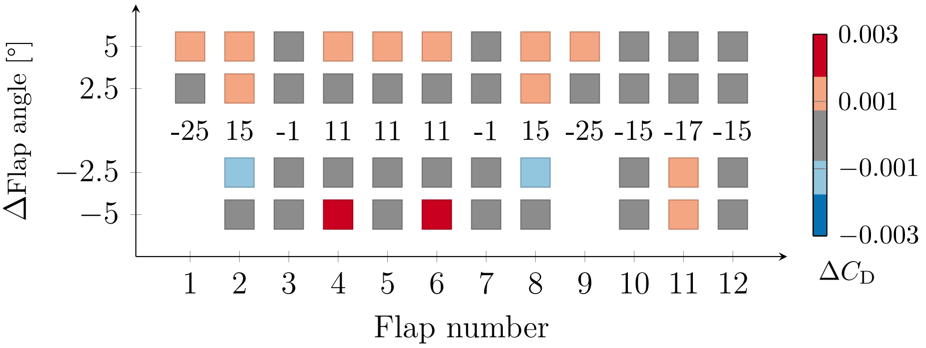

Figure 5.26: 0°*-yaw optimised design sensitivity to flap angle changes of each flap while keeping the other flap angles constant.*

constraint applied in the sensitivity analysis. The sensitivity analysis, illustrated in Figure 5.26, shows mainly increases in drag for the majority of the flaps, indicating that the optimised design is in a local optimum. Changes in drag less than the 95 % confidence interval are greyed out. The sides of the geometry are less sensitive to changes compared to the top and bottom. The roof flaps are the most sensitive to changes with mainly drag increases.

5.3.2 5° & 10°-yaw

The optimisation was performed for 5° and 10°-yaw with 433 and 206 designs tested respectively. In this section, it is primarily the results at 5°-yaw which are presented. Drag values for the 5° and 10°-yaw optimised asymmetric geometries are listed as Active opt. in Table 5.4. The drag value at each yaw angle as well as the uncertainty for the cycle averaged drag values are presented. The cycle

Configuration.	$C_{\mathrm{D},0}$	$C_{\mathrm{D},5}$	$C_{\mathrm{D},10}$	C_{DWC}
Smooth cav.	0.280	0.298	0.338	0.2952 ± 0.0005
0°-yaw opt.	0.263	0.296	0.334	0.2849 ± 0.0005
Active opt.	0.263	0.286	0.325	0.2803 ± 0.0005
Cycle ave. opt.	0.267	0.292	0.330	0.2852 ± 0.0005

Table 5.4: *Aerodynamic force coefficients at* 10°*-yaw.*

averaged drag values are within the uncertainty margin between the geometry optimised at 0°-yaw and the cycle averaged drag optimised geometry.

While the cycle averaged drag values are similar, the resulting designs differ. The crossflow for the designs at 5°-yaw is shown in Figure 5.27. The plane is measured normal to the tunnel flow while the vehicle is yawed on the turntable. The crossflow magnitude is relative to the vehicle coordinate system. A large rotating structure similar to the one found for the previously presented XC60 results with a 3/4 smooth cavity is found for the smooth cavity here as well. This creates a mainly downwash dominated wake as the vehicle is yawed. The downwash is reduced by the 0°-yaw optimised design and further reduced by the cycle averaged drag optimised design. This structure is not evident in the asymmetric 5°-yaw optimised design.

The 5°-yaw optimised design has a windward roof flap, position 4, which has a smaller angle than the other two roof flaps. This is the opposite behaviour to the positive roof flap on the leeward side of the Windsor flap optimisation results. The main difference between these results is the location of the rotating structure. For the full scale geometry, it is located on the windward side with a downwash dominated wake, while for the Windsor body it is located on the leeward side with a mainly upwash dominated wake.

Flap sensitivity to drag was also analysed at yaw, Figure 5.28. Some flaps, for example, flap 12, show no change in drag when adding 2.5° or 5°. This flap is likely separated at these high flap angles and is located near the wheel wake. As such, some of the flap angles in the optimised geometry bear little importance to the overall performance.

The design optimised at 10°-yaw is similar to the 5°-yaw optimised design and features the flap angles (3°, −13°, 5°, 25°, 25°, 25°, −25°, 25°, 25°, −19°, −25°, −25°). In large there are similarities, but most angles are larger and several are at the maximum position. This is likely due to the increasing downwash at yaw which requires larger flap angles as the yaw angle increases.

The smooth cavity, 0°-yaw optimised and the cycle averaged drag optimised design were tested for a full yaw sweep from −20° to 20°, Figure 5.29. Both the cycle averaged drag optimised and the 0°-yaw optimised designs have similar performance and, as shown in Table 5.4, have similar cycle averaged drag performance as well. It is only at 0°-yaw where the 0°-yaw optimised design outperforms the cycle averaged

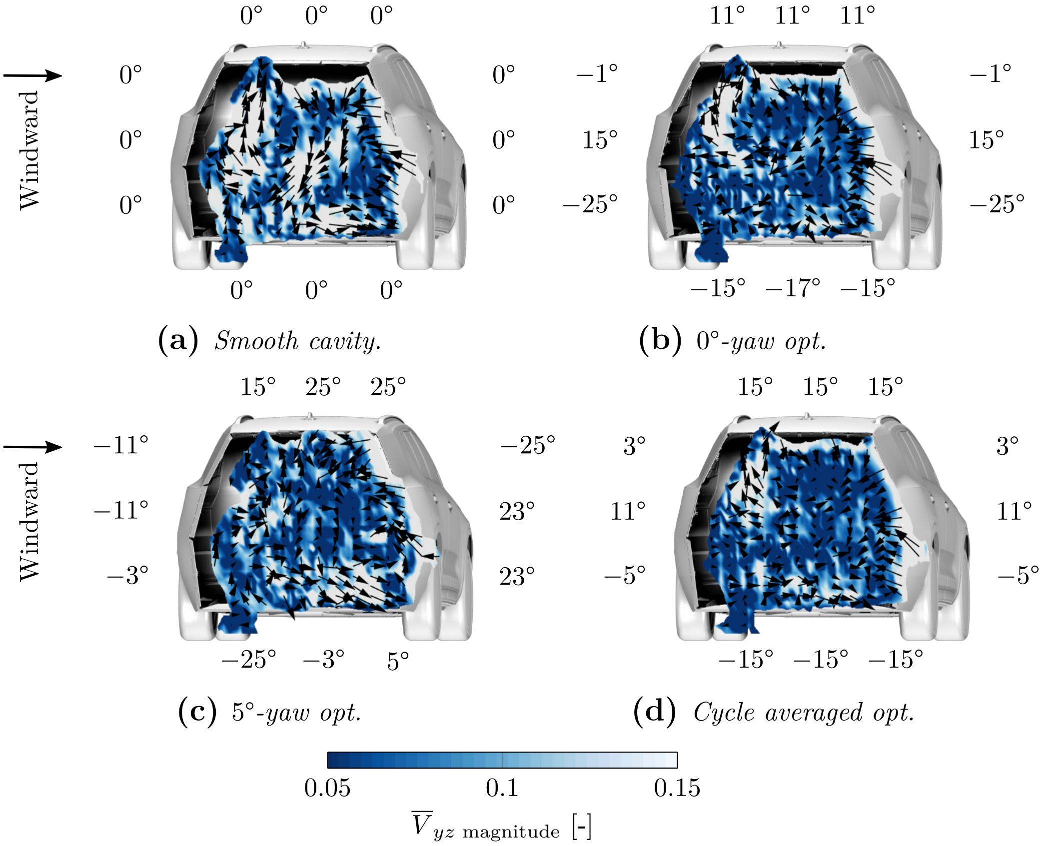

(a) *Smooth cavity.* (b) 0°*-yaw opt.*

(c) 5°*-yaw opt.* (d) *Cycle averaged opt.*

Figure 5.27: *Crossflow velocity magnitude behind the vehicle at* 5°*-yaw. The values are normalised by* V_∞ *and clipped where the total pressure coefficient is larger than 0.*

drag optimised design. A benefit of the cycle averaged optimised design is the reduction in lift over the entire range, improving stability. These results are in line with the results found by Howell [11] and Sterken et al. [27] for SUVs where a reduction in lift reduces the drag increase at yaw.

The sensitivity of the cycle averaged drag design was also investigated, Figure 5.30, showing low sensitivity to changes for the majority of the flaps. The greyed out confidence interval is smaller when the cycle averaged drag is calculated, 0.0005 C_D,

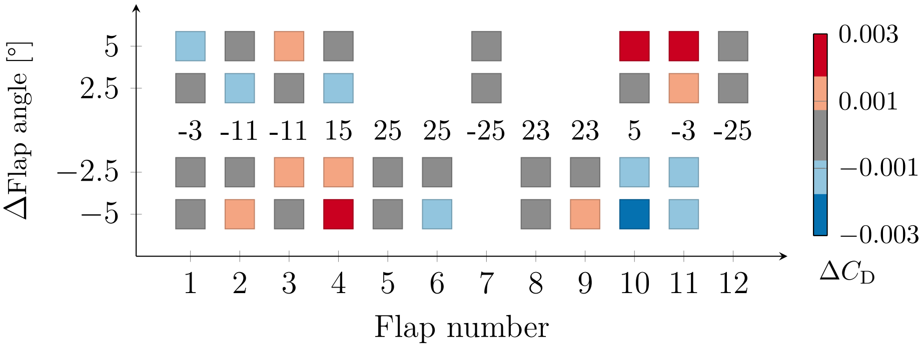

Figure 5.28: 5°*-yaw optimised design sensitivity to flap angle changes of each flap while keeping the other flap angles constant.*

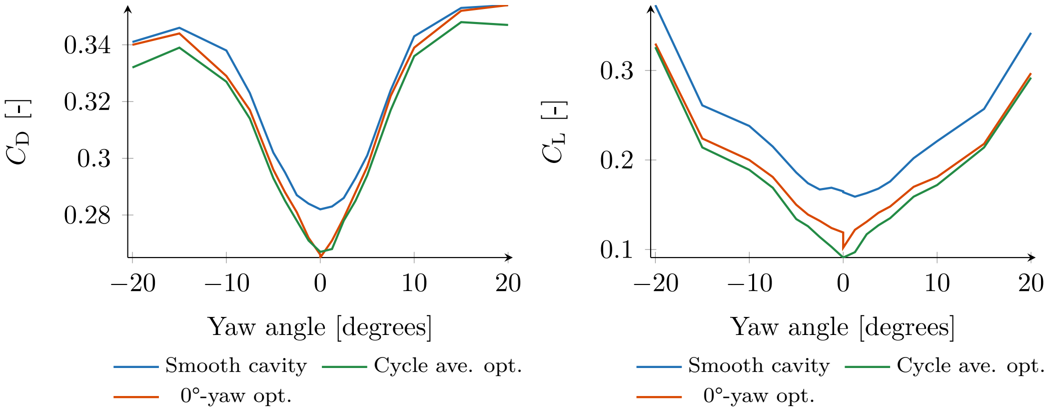

Figure 5.29: *Yaw sweep of the smooth cavity, 0°-yaw optimised and the cycle averaged drag optimised designs.*

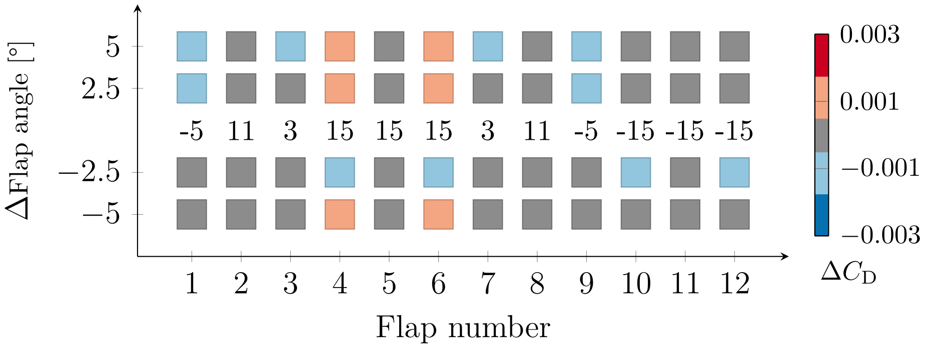

Figure 5.30: *Cycle averaged drag optimised design sensitivity to flap angle changes of each flap while keeping the other flap angles constant.*

as it is comprised of drag from three yaw angles. Overall, the sensitivity to change is low for any of the flaps investigated here. Compared to the 0°-yaw optimised design, the cycle averaged optimised design has a higher roof angle to counteract the downwash generated at yaw. There is also a larger difference in the bottom flaps on the sides, 1 and 9, and based on the sensitivity analysis, these designs benefit from the opposite movement. The −25° flap in this position for the 0°-yaw optimised design is expected to be separated and appears to be so based on the wake planes.

The base pressures, shown in Figure 5.31, are qualitatively similar for the smooth cavity, 0°-yaw optimised, and the cycle averaged optimised design with a high-pressure region near the lower windward corner and a low-pressure zone toward the leeward side. The 5°-yaw optimised design has a more uniform base pressure distribution with less difference between the high and low-pressure zones. The high-pressure zone is located toward the bumper and this likely extends outside of the measure region further down, lowering drag compared to the other designs.

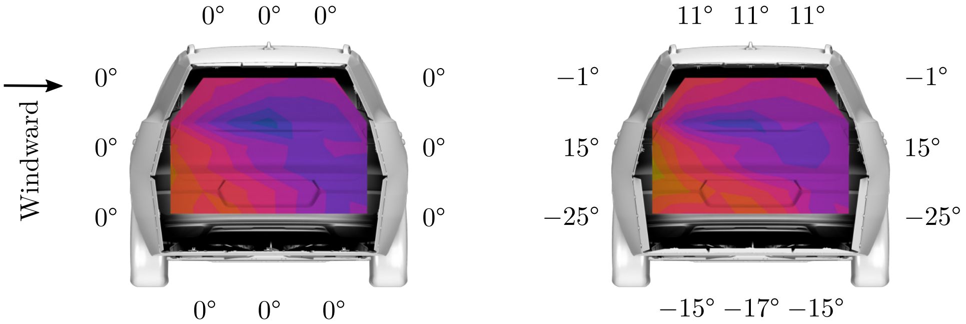

(a) *Smooth cavity.* **(b)** 0°-*yaw opt.*

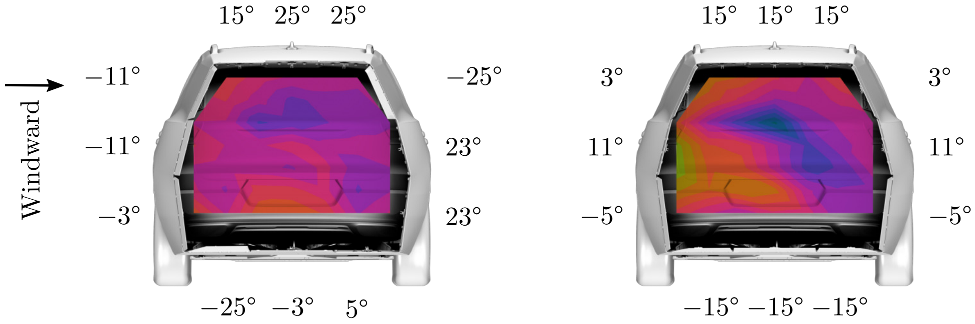

(c) 5°-*yaw opt.* **(d)** *Cycle averaged opt.*

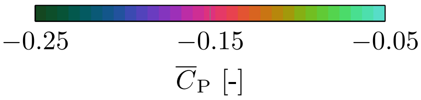

Figure 5.31: *Base pressure at* 5°-*yaw.*

5.4 Influence of wake balance at yaw

The wakes have been shown to become either upwash or downwash dominated as the vehicle is yawed. However, the reason why some wakes become upwash dominated while others become downwash dominated has yet to be explained. This section provides a possible reason for this effect.

Howell [11] found that boxier vehicle models like SUVs and hatchbacks benefit from a reduction in lift to reduce the drag penalty at yaw. This is consistent with the results in this thesis and is found to correlate well with the increased downwash as the model is yawed. This is the opposite reaction observed for the Windsor model which benefits from increases in lift to counteract the increased upwash at yaw. This behaviour was also found by Howell [11] for the Windsor body and is similar to the behaviour of saloon vehicles which benefit from an increase in lift to reduce the drag increase from yawing the vehicle.

The identified rotating wake structure and the reason for this structure to move from the windward side on the XC40 and XC60 to the leeward side of the Windsor body is not fully understood. However, the windward vortex originating near the roof for the Windsor body due to the sharp roof edge is not found in the full-scale results, Figure 5.32.

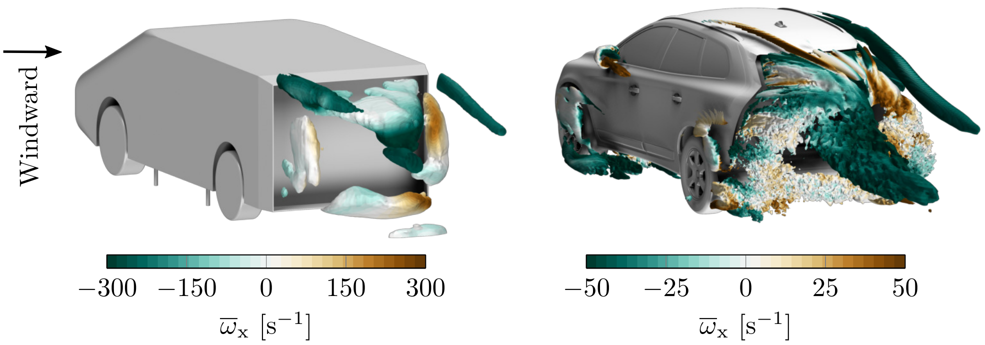

(a) *Windsor body smooth tapered cavity.* **(b)** *XC60 smooth cavity.*

Figure 5.32: $Q_{criterion}$ *at* 5°*-yaw. Windsor body ISO value* $10\,000\,\mathrm{s}^{-2}$*, XC60 ISO value* $350\,\mathrm{s}^{-2}$*. Negative vorticity relates to clockwise rotation.*

The more rounded corner of production vehicles may suppress the formation of this vortex. Wieser et al. [60] showed the windward vortex originating from the C-pillar of a generic notchback DrivAer vehicle at yaw. This is a sedan type shape which, as the Windsor body, benefits from increasing lift to reduce the drag increase at yaw. Both the windward C-pillar vortex of a sedan and the windward vortex at the sharp roof corner of the Windsor body are thought to have the same effect, delaying the formation of the large rotating wake structure to the leeward side of the wake, causing it to be upwash dominated as the vehicle is yawed. Rossitto et al. [61] investigated C-pillar rounding on a fastback vehicle where the C-pillar vortices were suppressed by the rear rounding. This also reduced the sensitivity to side wind while reducing lift at 10°-yaw. Reductions in lift are expected to increase the sensitivity to side wind based on the literature for this vehicle shape [11]. This strengthens the theory that the windward vortex, or lack thereof, interacts with the wake, causing the large rotating structure in the wake to be located further towards the leeward side of the base when the windward vortex is present.

Chapter 6

Concluding remarks

As shown previously in the literature, realistic operating conditions, such as the wind environment, have an impact on the aerodynamic drag of road vehicles. However, the available information on the complete wake flow at yaw is limited.

The objective of this thesis was to increase the knowledge of the wake structures at yaw and their relation to the vehicle's base pressure. This has been achieved through experimental and numerical investigations of generic model-scale geometry as well as detailed full-scale geometries.

A key part of the success in achieving this thesis objective is attributed to the use of optimisation algorithms as a tool to generate low-drag reference geometries for different yaw angles. A high performing surrogate model-based algorithm was developed in this work, suitable for problems with expensive cost functions, such as aerodynamic simulations or wind tunnel tests. The use of an optimisation algorithm resulted in geometries that, at first, were not expected to perform well and would not have been found by the author otherwise.

The most consistent trend for all configurations with low drag is a balanced wake where the recirculating flow in the wake is aligned with the vehicle. For a laterally symmetric wake without yawed flow, this means that the wake is neither upwash nor downwash dominated. The crossflow in the near wake is a good indicator of the wake balance where low crossflow is found for balanced, low drag, wakes. This is particularly useful at yaw where the lateral symmetry of the wake is lost.

The low-drag vehicles with improved wake balance generally have increased large scale coherent motions in the wake. This is ascribed to the wake being able to move more freely. The large scale coherent motions are reduced at yaw as the wake is pushed into a more stable, but higher drag, state that is either upwash or downwash dominated. Large scale unsteady motions have been linked to increases in drag in the literature. In this work, however, improving the wake balance was found to be the more important indicator of overall drag.

Optimising the geometry for several yaw angles using a cycle averaged drag coefficient resulted in designs where part of the performance without yaw was sacrificed to improve the design over a broader range of operating conditions. This signifies the importance of considering multiple flow conditions during vehicle development. The wake balance for the cycle averaged drag optimised geometries without yaw was shifted either up or down in the opposite direction to the additional up- or downwash experienced at yaw.

6.1 Future work

In this work, the wake was shown to become either upwash or downwash dominated at yaw. The reason could be linked to the windward vortex originating from the sharp top corner of the Windsor body and the lack of such a vortex for the full-scale geometries. There is not enough evidence yet to fully substantiate this link and requires further investigation.

The surrogate model optimisation algorithm developed in this project has good performance for expensive cost function. The information used in the surrogate model is the design parameters and the objective function value of each design. There is a lot more data available for both wind tunnel tests and numerical simulations which could be incorporated in the model. There is also potential to share knowledge between different optimisation campaigns, for example, the knowledge of wake balance could be used on a new vehicle to reduce the number of iterations required for previously unseen geometry. This could improve the performance further, however, the added flexibility needs to be balanced to prevent overfitting of the model.

The increased upwash or downwash of the wake at yaw can be mitigated by using a rear spoiler. Several production vehicles today are equipped with moveable spoilers. The potential benefit of actively controlling the spoiler angle to reduce drag needs to be balanced with the increased energy requirements and potential safety concerns regarding the aerodynamic lift. Metrological forecasts or accelerometer data could be used without the need for additional sensors to determine the spoiler position and be implemented through software changes on existing vehicles. Even a short wind tunnel measurement campaign to determine an appropriate cycle averaged drag spoiler position could reduce the real-world drag of existing vehicles. The net energy savings and appropriate control strategies need further investigation.

When performing the wind tunnel tests for the servo-controlled flaps, the drag would sometimes momentarily be reduced beyond the optimum when the flaps were moved from the optimum position to the inward position between designs. This indicates that there is further potential for drag reduction using unsteady methods. Unsteady flow control is a strategy that is known to reduce drag and there is extensive research on the topic. However, these methods are typically applied to an already high drag vehicle with an unbalanced wake. A question that remains is, could servo-controlled flaps provide additional benefit by unsteady control at small time scales, even when considering the energy consumption of the flap movement? Additionally, could other active flow control methods, such as suction or blowing, be combined with flaps to further reduce drag?

Chapter 7

Summary of papers

7.1 Paper I

Numerical analysis of a vehicle wake with tapered rear extensions under yaw conditions

The focus of the first paper is related to the objective of this thesis: to increase the knowledge of how vortical structures are related to the vehicles base pressure, especially at yaw and how it correlates to drag. A numerical investigation was performed of a fully detailed production vehicle with a tapered $^3/_4$ cavity subject to side wind. The cavity protrudes 150 mm from the base and is investigated in two configurations: with a smooth taper and a taper with an added kick. A smooth taper provided the greatest drag improvement without side wind while the cavity with a kick yielded an additional reduction at yaw. This reduces the vehicle's sensitivity to side wind by improving the wake balance of the vehicle. Unsteady influences from the cavity were found; however, the most consistent indicator of the performance in relation to drag was the wake balance.

7.2 Paper II

Surrogate-based optimisation using adaptively scaled Radial Basis Functions

The second paper features method development of an optimisation algorithm. The performance of two surrogate-based optimisation methods; a Proper Orthogonal Decomposition-based method and a force-based method. The generic passenger vehicle DrivAer was used to investigate the surrogate model's predictive ability where the force-based method outperformed the POD-based one. The surrogate model makes use of Radial Basis Function interpolation where the hyperparameters are optimised using differential evolution. An additional axis scaling factor was used and treated as a hyperparameter reducing the interpolation error by more than 50 %. The performance of the force-based surrogate model was compared with three other gradient-free optimisation techniques showing as good, or better performance, for 16 out of the 18 tested benchmark problems.

7.3 Paper III

Aerodynamic drag improvements on a square-back vehicle at yaw using a tapered cavity and asymmetric flaps

This paper investigates the use of trailing edge flaps on a modified version of the generic Windsor geometry with wheels and a rearward-facing base cavity in steady side wind conditions. The trailing edge flaps are distributed at the trailing edge of the cavity along the roof and sides totalling nine flaps. A surrogate model-based optimisation algorithm was used to minimise the drag coefficient by optimising the angle of each flap individually in the Loughborough University Large Wind Tunnel. The pressure measurements and tomographic Particle Image Velocimetry suggest that the optimised flap angles improve drag by reducing the strength of a large leeward side rotating structure in the wake, balancing the wake.

7.4 Paper IV

Drag reduction mechanisms on a generic square-back vehicle using an optimised yaw-insensitive base cavity

This paper investigates a base cavity on the Windsor geometry with wheels in the Loughborough University Large Wind Tunnel. The cavity angles have been optimised using numerical simulations to achieve a yaw-insensitive geometry. This is compared to a straight cavity and a filled tapered cavity to isolate the effects from the tapering and cavity. The design is analysed using pressure measurements and tomographic Particle Image Velocimetry. The results show an increased downwash of the optimised cavity without yaw to counteract the increase in upwash seen at yaw. The optimised cavity reduces the wake crossflow and results in a smaller wake with less losses. The overall wake unsteadiness is reduced by the cavity by minimising mixing in the shear layers. However, large scale coherent wake motions were increased by the investigated cavities as the wake became more balanced.

7.5 Paper V

Optimisation of trailing edge flaps on the base cavity of a vehicle for improved performance at yaw

The last paper focuses on a base cavity applied to a full-scale XC40 electric vehicle with twelve additional flaps applied to the trailing edge of the cavity. These flaps are controlled wirelessly using servos to allow continuous optimisation of the flap angles while maintaining the wind speed in the Volvo Cars Wind Tunnel. The results show that the wake becomes increasingly downwash dominated at yaw. One of the objectives was to reduce the cycle averaged drag which considers several weighted yaw angles. The cycle averaged drag optimised design becomes less sensitive to yaw by adding an upwash bias to the wake flow with the roof flaps at 0°-yaw. The slight upwash bias counteracts the increase in downwash at yaw while decreasing lift for the entire operating range. This, however, reduces the performance without side wind.

Bibliography

[1] M. Urquhart. *Vehicle wakes subject to side wind conditions*. en. Chalmers University of Technology, 2019. URL: https://research.chalmers.se/en/publication/511712 (visited on 05/20/2021).

[2] European Environment Agency. *Transport emissions of greenhouse gases*. 2019. URL: https://www.eea.europa.eu/data-and-maps/indicators/transport-emissions-of-greenhouse-gases/transport-emissions-of-greenhouse-gases-12 (visited on 06/16/2021).

[3] European Federation for Transport and Environment AISBL. *Mind the Gap 2016 - Report*. 2016. URL: https://www.transportenvironment.org/publications/mind-gap-2016-report (visited on 03/21/2019).

[4] U. Tietge et al. "FROM LABORATORY TO ROAD A 2015 update of official and "real-world" fuel consumption and CO2 values for passenger cars in Europe". In: (2015).

[5] J. Pavlovic, A. Marotta, and B. Ciuffo. "CO 2 emissions and energy demands of vehicles tested under the NEDC and the new WLTP type approval test procedures". en. In: *Applied Energy* 177 (Sept. 2016), pp. 661–670. ISSN: 03062619. DOI: 10.1016/j.apenergy.2016.05.110. URL: https://linkinghub.elsevier.com/retrieve/pii/S0306261916307152 (visited on 03/22/2019).

[6] Z. Yang and A. Bandivadekar. *2017 Global update: Light-duty vehicle greenhouse gas and fuel economy standards*. 2017. URL: https://www.theicct.org/publications/2017-global-update-LDV-GHG-FE-standards (visited on 03/20/2019).

[7] U. Tietge et al. *FROM LABORATORY TO ROAD: A 2018 UPDATE OF OFFICIAL AND "REAL-WORLD" FUEL CONSUMPTION AND CO2 VALUES FOR PASSENGER CARS IN EUROPE*. 2019. URL: https://theicct.org/sites/default/files/publications/Lab_to_Road_2018_fv_20190110.pdf (visited on 06/17/2021).

[8] J. Y. Wong. *Theory of ground vehicles*. en. 3rd ed. New York: John Wiley, 2001. ISBN: 978-0-471-35461-1.

[9] R. H. Barnard. *Road vehicle aerodynamic design : an introduction*. 3. ed. MechAero Pub., 2009. ISBN: 978-0-9540734-7-3.

[10] S. Windsor. "Real world drag coefficient – is it wind averaged drag?" en. In: *The International Vehicle Aerodynamics Conference*. Elsevier, 2014, pp. 3–17. ISBN: 978-0-08-100199-8. DOI: 10.1533/9780081002452.1.3. URL: https://linkinghub.elsevier.com/retrieve/pii/B9780081001998500010 (visited on 04/08/2019).

[11] J. Howell. “Aerodynamic Drag of Passenger Cars at Yaw”. en. In: *SAE International Journal of Passenger Cars - Mechanical Systems* 8.1 (Apr. 2015). ISSN: 1946-4002. DOI: 10.4271/2015-01-1559. URL: http://papers.sae.org/2015-01-1559/ (visited on 03/01/2018).

[12] T. C. Schuetz. *Aerodynamics of Road Vehicles, Fifth Edition*. English. 5 edition. Warrendale, Pennsylvania: SAE International, Dec. 2015. ISBN: 978-0-7680-7977-7.

[13] J. Gargoloff et al. “Robust Optimization for Real World CO2 Reduction”. en. In: May 2018. DOI: 10.4271/2018-37-0015. URL: https://www.sae.org/content/2018-37-0015/ (visited on 04/08/2019).

[14] J. Howell, D. Forbes, and M. Passmore. “A drag coefficient for application to the WLTP driving cycle”. en. In: *Proceedings of the Institution of Mechanical Engineers, Part D: Journal of Automobile Engineering* 231.9 (Aug. 2017), pp. 1274–1286. ISSN: 0954-4070, 2041-2991. DOI: 10.1177/0954407017704784. URL: http://journals.sagepub.com/doi/10.1177/0954407017704784 (visited on 03/01/2018).

[15] M. Varney, M. Passmore, and A. Gaylard. “Parametric Study of Asymmetric Side Tapering in Constant Cross Wind Conditions”. In: Apr. 2018. DOI: 10.4271/2018-01-0718. URL: http://www.sae.org/content/2018-01-0718/ (visited on 04/24/2018).

[16] D. Barros et al. “Bluff body drag manipulation using pulsed jets and Coanda effect”. en. In: *Journal of Fluid Mechanics* 805 (Oct. 2016), pp. 422–459. ISSN: 0022-1120, 1469-7645. DOI: 10.1017/jfm.2016.508. URL: https://www.cambridge.org/core/journals/journal-of-fluid-mechanics/article/bluff-body-drag-manipulation-using-pulsed-jets-and-coanda-effect/12609816D2FF77F5372BA9B3E32F69A8 (visited on 11/29/2018).

[17] E. G. Duell and A. R. George. “Experimental Study of a Ground Vehicle Body Unsteady Near Wake”. In: *International Congress & Exposition*. SAE International, 1999. DOI: https://doi.org/10.4271/1999-01-0812. URL: https://doi.org/10.4271/1999-01-0812.

[18] G. Pavia et al. “Salient three-dimensional features of the turbulent wake of a simplified square-back vehicle”. en. In: *Journal of Fluid Mechanics* 888 (Apr. 2020), A33. ISSN: 0022-1120, 1469-7645. DOI: 10.1017/jfm.2020.71. URL: https://www.cambridge.org/core/product/identifier/S0022112020000713/type/journal_article (visited on 03/18/2020).

[19] S. Bonitz. *Development of Separation Phenomena on a Passenger Car*. en. Chalmers University of Technology, 2018. ISBN: 978-91-7597-785-0. URL: https://research.chalmers.se/en/publication/510047 (visited on 05/04/2019).

[20] A. Evrard et al. “Fluid force and symmetry breaking modes of a 3D bluff body with a base cavity”. In: *J. Fluids Struct.* 61 (2016), pp. 99–114. ISSN: 08899746. DOI: 10.1016/j.jfluidstructs.2015.12.001. URL: https://linkinghub.elsevier.com/retrieve/pii/S0889974615002698.

[21] E. G. Duell and a. R. George. “Measurements in the Unsteady Near Wakes of Ground Vehicle Bodies”. In: *SAE Tech. Pap.* SAE International, 1993. ISBN: 4230824815. DOI: 10.4271/930298. URL: http://www.sae.org/technical/papers/930298.

[22] G. Bonnavion et al. “Asymmetry and global instability of real minivans’ wake”. en. In: *Journal of Wind Engineering and Industrial Aerodynamics* 184 (Jan. 2019), pp. 77–89. ISSN: 01676105. DOI: 10.1016/j.jweia.2018.11.006. URL: https://linkinghub.elsevier.com/retrieve/pii/S0167610518307578 (visited on 02/19/2019).

[23] S.R. Ahmed, G. Ramm, and G. Faltin. “Some Salient Features Of The Time-Averaged Ground Vehicle Wake”. In: (1984). ISSN: 0148-7191. DOI: https://doi.org/10.4271/840300. URL: https://doi.org/10.4271/840300.

[24] K. R. Cooper. “The Effect of Front-Edge Rounding and Rear-Edge Shaping on the Aerodynamic Drag of Bluff Vehicles in Ground Proximity”. In: *SAE International Congress and Exposition.* SAE International, Feb. 1985. DOI: https://doi.org/10.4271/850288.

[25] A. K. Perry. “An investigation into the base pressure of simplified automotive squareback geometries”. PhD thesis. Loughborough University, 2016. URL: https://dspace.lboro.ac.uk/2134/22605.

[26] G. Pavia and M. Passmore. “Characterisation of Wake Bi-stability for a Square-Back Geometry with Rotating Wheels”. In: *Prog. Veh. Aerodyn. Therm. Manag.* Ed. by Jochen Wiedemann. Cham: Springer International Publishing, 2018, pp. 93–109. ISBN: 978-3-319-67822-1. DOI: 10.1007/978-3-319-67822-1_6.

[27] L. Sterken et al. “Effect of Rear-End Extensions on the Aerodynamic Forces of an SUV”. In: *SAE Technical Papers.* Apr. 1, 2014. DOI: 10.4271/2014-01-0602. URL: http://papers.sae.org/2014-01-0602/ (visited on 11/30/2016).

[28] S. Sebben, L. Sterken, and T. Wölken. “Characterization of the rear wake of a sport utility vehicle with extensions and without extensions”. In: *Institution of Mechanical Engineers, Part D: Journal of Automobile Engineering* (2016). DOI: DOI:10.1177/0954407016678016.

[29] L. Sterken et al. “Wake and Unsteady Surface-Pressure Measurements on an SUV with Rear-End Extensions”. In: *SAE Technical Papers.* Apr. 14, 2015. DOI: 10.4271/2015-01-1545. URL: http://papers.sae.org/2015-01-1545/ (visited on 11/30/2016).

[30] *Vehicle Aerodynamics Terminology (J1594 Ground Vehicle Standard) - SAE Mobilus*. URL: https://saemobilus.sae.org/content/j1594_199412 (visited on 05/21/2019).

[31] G. Johl. "The design and performance of a 1.9m x 1.3m indraft wind tunnel". PhD thesis. Loughborough University, 2010.

[32] D. Wood. "The Effect of Rear Geometry Changes on the Notchback Flow Field". PhD thesis. Loughborough University, 2015.

[33] M. Varney. "Base drag reduction for squareback road vehicles". en. thesis. Loughborough University, Feb. 2020. DOI: 10.26174/thesis.lboro.11823759.v1. URL: https://repository.lboro.ac.uk/articles/Base_drag_reduction_for_squareback_road_vehicles/11823759 (visited on 03/18/2020).

[34] G. E. Elsinga et al. "On the velocity of ghost particles and the bias errors in Tomographic-PIV". In: *Exp. Fluids* 50.4 (2011), pp. 825–838. ISSN: 1432-1114. DOI: 10.1007/s00348-010-0930-0.

[35] J. Sternéus, T. Walker, and T. Bender. "Upgrade of the Volvo Cars Aerodynamic Wind Tunnel". In: *SAE World Congress & Exhibition*. SAE International, 2007. DOI: https://doi.org/10.4271/2007-01-1043. URL: https://doi.org/10.4271/2007-01-1043.

[36] Aeroprobe. *Omniprobe*. 2018. URL: http://www.aeroprobe.com/omniprobe/ (visited on 05/21/2021).

[37] E. Ljungskog. *Evaluation and modeling of the flow in a slotted wall wind tunnel*. en. Chalmers University of Technology, 2019. ISBN: 978-91-7905-219-5. URL: https://research.chalmers.se/en/publication/514006 (visited on 05/21/2021).

[38] T. Hobeika and S. Sebben. "CFD investigation on wheel rotation modelling". In: *Journal of Wind Engineering and Industrial Aerodynamics* 174 (Mar. 2018), pp. 241–251. ISSN: 01676105. DOI: 10.1016/j.jweia.2018.01.005. URL: http://linkinghub.elsevier.com/retrieve/pii/S0167610517307286 (visited on 03/15/2018).

[39] P. Ekman et al. "Accuracy and Speed for Scale-Resolving Simulations of the DrivAer Reference Model". In: Apr. 2019, pp. 2019–01–0639. DOI: 10.4271/2019-01-0639. URL: https://www.sae.org/content/2019-01-0639/ (visited on 05/22/2021).

[40] L. Davidson. "Large Eddy Simulations: How to evaluate resolution". In: *International Journal of Heat and Fluid Flow* 30.5 (2009). The 3rd International Conference on Heat Transfer and Fluid Flow in Microscale, pp. 1016–1025. ISSN: 0142-727X. DOI: https://doi.org/10.1016/j.ijheatfluidflow.2009.06.006. URL: http://www.sciencedirect.com/science/article/pii/S0142727X09001039.

[41] S. J. Bates, J Sienz, and V. Toropov. "Formulation of the Optimal Latin Hypercube Design of Experiments Using a Permutation Genetic Algorithm". In: 2011 (Apr. 2004). DOI: 10.2514/6.2004-2011.

[42] A.-K. Perry, G. Pavia, and M. Passmore. “Influence of short rear end tapers on the wake of a simplified square-back vehicle: wake topology and rear drag”. In: *Experiments in Fluids* 57.11 (Nov. 1, 2016), p. 169. ISSN: 0723-4864, 1432-1114. DOI: 10.1007/s00348-016-2260-3. URL: http://link.springer.com/article/10.1007/s00348-016-2260-3 (visited on 11/30/2016).

[43] Y. Wang et al. “Experimental study of wheel-vehicle aerodynamic interactions”. en. In: *Journal of Wind Engineering and Industrial Aerodynamics* 198 (Mar. 2020), p. 104062. ISSN: 0167-6105. DOI: 10.1016/j.jweia.2019.104062. URL: http://www.sciencedirect.com/science/article/pii/S0167610519306622 (visited on 04/02/2020).

[44] J. B. Fuller. “The unsteady aerodynamics of static and oscillating simple automotive bodies”. en. thesis. Loughborough University, Jan. 2012. URL: https://repository.lboro.ac.uk/articles/thesis/The_unsteady_aerodynamics_of_static_and_oscillating_simple_automotive_bodies/9217136/1 (visited on 11/10/2020).

[45] M. Grandemange, M. Gohlke, and O. Cadot. “Bi-stability in the turbulent wake past parallelepiped bodies with various aspect ratios and wall effects”. en. In: *Physics of Fluids* 25.9 (Sept. 2013), p. 095103. ISSN: 1070-6631, 1089-7666. DOI: 10.1063/1.4820372. URL: http://aip.scitation.org/doi/10.1063/1.4820372 (visited on 09/09/2020).

[46] Y. Haffner et al. “Mechanics of bluff body drag reduction during transient near-wake reversals”. en. In: *Journal of Fluid Mechanics* 894 (July 2020), A14. ISSN: 0022-1120, 1469-7645. DOI: 10.1017/jfm.2020.275. URL: https://www.cambridge.org/core/product/identifier/S002211202000275X/type/journal_article (visited on 09/17/2020).

[47] G. Pavia, M. Passmore, and C. Sardu. “Evolution of the bi-stable wake of a square-back automotive shape”. In: *Exp. Fluids* 59.1 (Dec. 2018), pp. 1–20. ISSN: 07234864. DOI: 10.1007/s00348-017-2473-0.

[48] A. K. Perry et al. “The study of a bi-stable wake region of a generic Squareback vehicle using Tomographic PIV”. In: *SAE World Congr.* (2016). ISSN: 1946-4002. DOI: 10.4271/2016-01-1610.

[49] M. Grandemange, O. Cadot, and M. Gohlke. “Reflectional symmetry breaking of the separated flow over three-dimensional bluff bodies”. en. In: *Physical Review E* 86.3 (Sept. 2012), p. 035302. ISSN: 1539-3755, 1550-2376. DOI: 10.1103/PhysRevE.86.035302. URL: https://link.aps.org/doi/10.1103/PhysRevE.86.035302 (visited on 09/09/2020).

[50] M. Grandemange, M. Gohlke, and O. Cadot. “Turbulent wake past a three-dimensional blunt body. Part 2. Experimental sensitivity analysis”. en. In: *Journal of Fluid Mechanics* 752 (Aug. 2014), pp. 439–461. ISSN: 0022-1120, 1469-7645. DOI: 10.1017/jfm.2014.345. URL: http://www.journals.cambridge.org/abstract_S0022112014003450 (visited on 01/02/2018).

[51] R. Li et al. “Feedback control of bimodal wake dynamics”. en. In: *Experiments in Fluids* 57.10 (Oct. 2016), p. 158. ISSN: 0723-4864, 1432-1114. DOI: 10.1007/s00348-016-2245-2. URL: http://link.springer.com/10.1007/s00348-016-2245-2 (visited on 12/05/2019).

[52] P. W. Bearman. “Investigation of the flow behind a two-dimensional model with a blunt trailing edge and fitted with splitter plates”. en. In: *Journal of Fluid Mechanics* 21.02 (Feb. 1965), p. 241. ISSN: 0022-1120, 1469-7645. DOI: 10.1017/S0022112065000162. URL: http://www.journals.cambridge.org/abstract_S0022112065000162 (visited on 05/03/2019).

[53] S. Luckhurst et al. “Computational investigation into the sensitivity of a simplified vehicle wake to small base geometry changes”. en. In: *Journal of Wind Engineering and Industrial Aerodynamics* 185 (Feb. 2019), pp. 1–15. ISSN: 0167-6105. DOI: 10.1016/j.jweia.2018.12.010. URL: http://www.sciencedirect.com/science/article/pii/S0167610518307244 (visited on 09/28/2020).

[54] J. Nagawkar, L. T. Leifsson, and X. Du. “Applications of Polynomial Chaos-Based Cokriging to Aerodynamic Design Optimization Benchmark Problems”. In: *AIAA Scitech 2020 Forum*. _eprint: https://arc.aiaa.org/doi/pdf/10.2514/6.2020-0542. American Institute of Aeronautics and Astronautics, Jan. 2020. DOI: 10.2514/6.2020-0542. URL: https://arc.aiaa.org/doi/abs/10.2514/6.2020-0542 (visited on 02/17/2021).

[55] K. Taira et al. “Modal Analysis of Fluid Flows: An Overview”. In: *arXiv:1702.01453 [physics]* (Feb. 5, 2017). arXiv: 1702.01453. URL: http://arxiv.org/abs/1702.01453.

[56] T. W. Muld, G. Efraimsson, and D. S. Henningson. “Mode Decomposition on Surface-Mounted Cube”. In: *Flow, Turbulence and Combustion* 88.3 (Apr. 2012), pp. 279–310. ISSN: 1386-6184, 1573-1987. DOI: 10.1007/s10494-011-9355-y. URL: http://link.springer.com/10.1007/s10494-011-9355-y (visited on 12/11/2017).

[57] R. Buchheim, K.-R. Deutenbach, and H.-J. Lückoff. “Necessity and Premises for Reducing the Aerodynamic Drag of Future Passenger Cars”. In: *SAE Transactions* 90 (1981). Publisher: SAE International, pp. 758–771. ISSN: 0096-736X. URL: https://www.jstor.org/stable/44631713 (visited on 05/25/2021).

[58] J. Marcos Garcia de la Cruz, Rowan D. Brackston, and Jonathan F. Morrison. “Adaptive Base-Flaps Under Variable Cross-Wind”. en. In: Aug. 2017. DOI: 10.4271/2017-01-7000. URL: http://www.sae.org/content/2017-01-7000/ (visited on 10/02/2018).

[59] L. Sterken et al. “Effect of the traversing unit on the flow structures behind a passenger vehicle”. en. In: *IMechE International Vehicle Aerodynamics Conference* (2014). ISBN: 9780081001998. URL: https://research.chalmers.se/en/publication/217295 (visited on 06/01/2021).

[60] D. Wieser, C. N. Nayeri, and C. O. Paschereit. “Wake Structures and Surface Patterns of the DrivAer Notchback Car Model under Side Wind Conditions”. en. In: *Energies* 13.2 (Jan. 2020), p. 320. ISSN: 1996-1073. DOI: 10.3390/en13020320. URL: https://www.mdpi.com/1996-1073/13/2/320 (visited on 06/02/2021).

[61] G. Rossitto et al. “Aerodynamic performances of rounded fastback vehicle”. In: *Proceedings of the Institution of Mechanical Engineers, Part A: Journal of Power and Energy* (Jan. 2017). Publisher: SAGE Publications, pp. 1211–1221. DOI: 10.1177/0954407016681684. URL: https://hal.archives-ouvertes.fr/hal-01449542 (visited on 06/14/2021).